Chemical Engineering Integrated Masters' Programme

Analysis of flow in branched stent-grafts for endovascular repair of the aortic arch

Master Thesis

by

Ana Margarida Outeirinho Morgado

Developed within the Dissertation course

held in the

Biofluids and Transport Group of the Separation and Transport Laboratory
Department of Chemical Engineering
Imperial College London

Imperial College
London

Supervisor at Imperial College London: **Professor Xiao Yun Xu**

Supervisor at FEUP: **Professor João Moreira de Campos**

U. PORTO
FEUP FACULDADE DE ENGENHARIA
UNIVERSIDADE DO PORTO

Department of Chemical Engineering

July 2015

Acknowledgements

To Professor Xiao Yun Xu, for the opportunity.

To Professor João Campos, for the encouragement and the guidance.

To Harkamaljot Kandail (Rocky), for the time, knowledge and patience.

To the $\chi\mu$ group, for the friendly work environment.

To Ana Fumega and Ana Soares – “Dissertações ao ataque!” -, for all the knowledge, support and jokes exchanged.

To Mamã, Papá, and Henri, no justifications being needed.

Resumo

A interação entre o escoamento do sangue e as paredes das artérias promove, frequentemente, o aparecimento de doenças vasculares. No caso da crossa da aorta, o procedimento convencional para estas patologias é a cirurgia aberta, cuja taxa de mortalidade é de 7 a 17 %. Uma alternativa aliciante à cirurgia, por se tratar de um procedimento menos invasivo, é a reparação aórtica endovascular, que consiste na introdução de um *stent-graft* através de uma artéria de acesso.

Estudos experimentais e numéricos têm contribuído para uma maior e melhor compreensão das doenças cardiovasculares, assim como para o desenvolvimento de técnicas de diagnóstico e *stent-grafts* de melhor desempenho.

Este trabalho consistiu no estudo numérico do escoamento sanguíneo num modelo tridimensional simplificado da crossa da aorta, com os seus três vasos superiores, antes e depois da introdução de um *stent-graft* ramificado. Verificou-se que a introdução do *stent-graft* aumenta a perfusão sanguínea através das três artérias superiores. Verificou-se, também, um aumento da tensão de corte nas paredes dos vasos, o que pode resultar em complicações pós-operatórias, *e.g.*, migração do dispositivo.

Foi testada uma nova metodologia para estabelecer uma condição fronteira resistiva, que consiste na extensão do modelo da crossa da aorta por um tubo constritivo, o qual impõe sobre o domínio a resistência da restante vasculatura. As principais caraterísticas fisiológicas do escoamento foram estudadas, após as simulações. Verificou-se uma diminuição da magnitude do caudal, possivelmente devida ao facto da curvatura da crossa da aorta não ter sido considerada. Os valores da resistência mantiveram-se constantes em todas as simulações.

Três *stent-grafts* ramificados foram testados, de forma a avaliar o impacto do diâmetro dos seus ramos no desempenho dos dispositivos. Foi identificada uma zona de recirculação no *bypass* da subclávia esquerda através da carótida esquerda comum. Apesar do uso de um *stent-graft* personalizado garantir melhor desempenho, de modo a reduzir os atrasos e os custos associados à sua produção, deve ser dada preferência a dispositivos cujo diâmetro dos ramos seja ligeiramente superior ao das artérias.

Palavras Chave: reparação aórtica endovascular; crossa da aorta; *stent-grafts* ramificados; dinâmica de fluidos computacional; condições fronteira resistivas.

Abstract

Vascular pathologies may arise from the interaction between blood flow and arteries walls. In the case of aortic arch diseases, the conventional open surgery procedure has a reported mortality rate of 7 – 17 %. Endovascular aortic repair, consisting in the introduction of a stent-graft through an access artery, constitutes an appealing alternative, being a less invasive procedure.

Haemodynamic studies performed both experimentally and numerically, have shed significant light over the characteristics of blood flow, leading to a better understanding of cardiovascular diseases and to the development of diagnosis tools and stent-grafts of improved performance.

In this work, numerical flow studies in simplified three-dimensional models of the aortic arch and three upper branches, before and after the introduction of an idealized branched stent-graft, were performed. The presence of the stent-grafts increases blood perfusion through the three supra-aortic vessels. Nevertheless, wall shear stress increases drastically after the introduction of the stent-graft, which may result in post-operative complications.

A new methodology for a resistance type outflow boundary condition, consisting in the attachment of a constriction tube to the outlets of the models, imposing the resistance of the downstream vasculature, was also tested. Using this methodology, the main physiological flow features are captured. A decrease in the flow rate magnitude is observed, possibly due to the absence of the arch's curvature. The specific resistance held constant for all simulations.

Three branched stent-grafts were tested, in order to evaluate the impact of the diameter of the stent-graft's branches in its hemodynamic performance. A persistent flow recirculation zone, FRZ, was identified in the bypass of the left subclavian artery through the left common carotid. Results suggested that, although the best haemodynamic performance would be achieved with customized branched stent-grafts, in order to minimize delays and costs, preference should be given to branches with slightly higher diameters than the ones of the vessels as these yield smaller FRZ.

Key-words: endovascular aortic repair; aortic arch; branched stent-graft; computational fluid dynamics; resistance boundary condition.

Statement

I hereby declare that this is an original work and that all non-original contributions needed to its completion were dully referenced with the respective source clearly identified.

Ana Morgado

July 2015

Table of Contents

1 Introduction 1
1.1 Motivation 1
1.2 Research question 2
1.3 Objectives 3
1.4 Thesis layout 3
2 State-of-the-Art 5
2.1 The aortic arch 5
2.2 Endovascular repair of the aortic arch 6
2.3 Modelling blood flow using Computational Fluid Dynamics 9
2.3.1 Problem Identification 9
2.3.2 Pre-processing 10
2.3.3 Solving 16
2.3.4 Post-processing 16
3 Methodology 17
3.1 Geometries 17
3.2 Mathematical flow modelling 19
3.3 Numerical flow modelling 20
3.3.1 Resistance type outflow boundary condition 20
3.3.2 Flow analysis in the branched stent-grafts 25
4 Results and Discussion 29
4.1 Results 29
4.1.1 *Calibration case vs. Reference case* 29
4.1.2 Reference case: uniform velocity profile *vs.* Womersley velocity profile 32
4.1.3 Branched stent-grafts for the aortic arch 34
4.2 Discussion 41
4.2.1 Resistance type outflow boundary condition 41
4.2.2 Branched stent-grafts for the aortic arch 42

5 Conclusions 45
    5.1 Main conclusions 45
    5.2 Limitations and Future work 46
    5.3 Global statement 46
References 47
Appendix 51
    I. Tables 51
    II. Calculations 52

List of Figures

Figure 1 – The heart and its main vessels, with focus on the ascending aorta, the aortic arch, the brachiocephalic trunk or innominate artery, IA, the left common carotid, LCCA, and the left subclavian artery, LSCA. *6*

Figure 2 - Anatomical landing zone map [13]. *7*

Figure 3 – (A) Schematic representation of a aortic arch branched stent-graft with a branch for the innominate artery and occlusion of both the left common carotid and left subclavian arteries [16]. (B) Precurved fenestrated stent-graft for the aortic arch with fenestration for the three supra-aortic vessels [18]. *8*

Figure 4 – Schematic drawing of the stent-graft prototype suggested by Finlay et al. [5]. A to E_2*: geometric parameters based on frequency measurements of the aortic arch mapping.* *9*

Figure 5 – Stability diagram showing in vivo disturbed and undisturbed flow data [34]. *13*

Figure 6 – Straight vessel with a rigid contraction tube [40]. *15*

Figure 7 – Fluid domain. An artificially model of the aortic arch was selected as the fluid domain, ΩF*. The idealized geometry was reconstructed with the physiological dimensions reported by Finlay et al. [5].* *17*

Figure 8 – Modified geometries for the fluid domain, ΩF*, including a branched stent-graft consisting of a main body and two tunnel stent-grafts for the innominate, IA, and the left common carotid, LCCA, arteries. (A) stent-graft 1; (B) stent-graft 2; (C) stent-graft 3.* *18*

Figure 9 – Rigid constriction tube representing the resistance type outflow boundary model. *20*

Figure 10 – Volumetric flow rate waveform at the ascending thoracic aorta. The flow waveform was extracted from Xiao [39], and corresponds to patient data acquired via Phase-Contrast MRI of a healthy 28 year-old male subject. *21*

Figure 11 – Volumetric flow rate waveform at the innominate artery, IA. The flow waveform was extracted from Xiao [39], and corresponds to patient data acquired via Phase-Contrast MRI of a healthy 28 year-old male subject. *21*

Figure 12 - Volumetric flow rate waveform at the left common carotid artery, LCCA. The flow waveform was extracted from Xiao [39], and corresponds to patient data acquired via Phase-Contrast MRI of a healthy 28 year-old male subject. *21*

Figure 13 - Volumetric flow rate waveform at the left subclavian artery, LSCA. The flow waveform was extracted from Xiao [39], and corresponds to patient data acquired via Phase-Contrast MRI of a healthy 28 year-old male subject. *22*

Figure 14 – Schematic of the computational model adopted in this work in order to obtain the boundary conditions for the calibration of the constriction tubes. At the inlet and outlets of the model, the boundary conditions prescribed are represented. *22*

Figure 15 – Experimental relationship between the ratio of the outlet and inlet diameters, γ_i, and the outlet pressure for the constriction tubes for: (A) innominate artery, (B) left common carotid artery, (C) left subclavian artery, and (D) descending aorta. A second order polynomial trend line (dashed line) was used to establish the relationship between both variables..23

Figure 16 – Schematic of the fully defined CFD model, $\Omega_{F,\mathrm{final}}$, for all geometries: (A) the aortic arch model, and the aortic arch model including the branched stent-graft: (B) stent-graft 1, (C) stent-graft 2, and (D) stent-graft 3.The black boxes highlight the constriction tubes...........................24

Figure 17 – Stability diagram [34]. Representing the peak systole Reynolds number, Re, against the Womersley parameter, α, determined at the inlet (intersection of the red horizontal and vertical lines) yields a point in the laminar flow region. 27

Figure 18 – Flow rate waveforms prescribe in the calibration case from patient PC-MRI data (on the left) and those obtained in the reference case (on the right), for the three supra-aortic vessels. Results are presented over one cardiac cycle (0.76 s)...30

Figure 19 – Blood inflow split into the four outlets of the aortic arch model for the calibration and reference cases...30

Figure 20 - Mean volumetric flow rate at the four outlets of the aortic arch model for the calibration and reference cases. 31

Figure 21 - Pressure waveforms at the four outlets of the aortic arch model, for the calibration and reference cases. Results are presented over a cardiac cycle (0.76 s)..31

Figure 22 – Flow rate waveforms at the four outlets of the aortic arch model, for a uniform and for a Womersley velocity profiles at the inlet (reference case). Results are presented over a cardiac cycle (0.76 s). 32

Figure 23 - Mean volumetric flow rate at the four outlets of the aortic arch model, for a uniform velocity profile and for a Womersley velocity profile at the inlet (reference case). 33

Figure 24 – Blood inflow split into the four outlets of the aortic arch model, for a uniform velocity profile and for a Womersley velocity profile at the inlet (reference case).................................33

Figure 25 – Specific resistance for all outlets of the aortic arch model, for a uniform velocity profile and for a Womersley velocity profile at the inlet (reference case)...34

Figure 26 - Flow rate waveforms at the four outlets of the aortic arch models for the reference case and for the three geometries including a branched stent-graft: (A) stent-graft 1, (B) stent -graft 2, (C) stent-graft 3. 34

Figure 27 - Blood inflow split into the four outlets of the aortic arch models for the reference case and for the three geometries including a branched stent-graft: (A) stent-graft 1, (B) stent-graft 2, (C) stent-graft 3. 35

Figure 28 – Mean volumetric flow rate at the four outlets of the aortic arch models for the reference case and for the three geometries including a branched stent-graft: (A) stent-graft 1, (B) stent--graft 2, (C) stent-graft 3. 35

Figure 29 - Specific resistance for all outlets of the aortic arch models for the reference case and for the three geometries including a branched stent-graft: (A) stent-graft 1, (B) stent-graft 2, (C) stent--graft 3. 36

Figure 30 - Time-averaged wall shear stress, TAWSS, contours for the models of the aortic arch (A) without stent-graft, and including the branched stent-graft: (B) stent-graft 1, (C) stent-graft 2, (D) stent-graft 3. The arrows mark flow recirculation zones found in the bypass of the LSCA through the LCCA, which are regions of low TAWSS. 37

Figure 31 – Time-points over the cardiac cycle. 37

Figure 32 - Velocity streamlines during peak systole ($t = 0.11$ *s) observed in the models of the aortic arch (A) without stent-graft, and including the branched stent-graft: (B) stent-graft 1, (C) stent--graft 2, (D) stent-graft 3.* 38

Figure 33 – Velocity streamlines during mid-deceleration time point ($t = 0.21$ *s) observed in the models of the aortic arch (A) without stent-graft, and including the branched stent-graft: (B) stent--graft 1, (C) stent-graft 2, (D) stent-graft 3.* 38

Figure 34 - Velocity vectors highlighting the flow recirculation zones, FRZ, found in the models of the aortic arch (A) without stent-graft, and including the branched stent-graft: (B) stent-graft 1, (C) stent-graft 2, (D) stent-graft 3, at $t = 0.21$ *s.* 39

Figure 35 – Velocity vectors highlighting the separation and reattachment points of the flow recirculation zone, FRZ, at $t = 0.21$ *s, in the bypass region of the three geometries including a branched stent-graft: (A) stent-graft 1, (B) stent-graft 2, (C) stent-graft 3.* 40

Figure 36 – Lengths of the flow recirculation zone, FRZ, found in the bypass of the LSCA through the LCCA in the geometries including a branched stent-graft: (A) stent-graft 1, (B) stent-graft 2, (C) stent--graft 3. 40

List of Tables

Table A. 1 - Dimension of the geometric parameters used to describe the fluid domain. Models of the aortic arch including stent-graft: (A) stent-graft 1, (B) stent-graft 2, (C) stent-graft 3. 51

Table A. 2 - Mesh statistics for all geometries: (A) the aortic arch model without stent-graft, and the models including the branched stent-graft: (B) stent-graft 1, (C) stent-graft 2, (D) stent-graft 3......52

Notation and Glossary

a	Radius	m
C	Compliance	m^3.Pa^{-1}
d	Diameter	m
D_1	Inlet diameter of the constriction tube	m
D_2	Outlet diameter of the constriction tube	m
K	Impedance	Ω
L_1	Length of the largest section of the constriction tube	m
L_2	Length of the narrowest section of the constriction tube	m
p	Pressure	Pa
$\bar{p}$	Mean pressure	Pa
Q	Volumetric flow rate	m^3.s
$\bar{Q}$	Mean volumetric flow rate	m^3.s
$\hat{Q}$	Volumetric flow rate at peak systole	m^3.s
R	Resistance	kg.m^{-4}.s^{-1}
R_1	Proximal resistance	kg.m^{-4}.s^{-1}
R_2	Distal resistance	kg.m^{-4}.s^{-1}
Re	Reynolds number	
$\widehat{\mathrm{Re}}$	Reynolds number at peak systole	
S	Cross-sectional area	m^2
t	Time	s
u	Velocity	m.s^{-1}
$\bar{u}$	Mean velocity	m.s^{-1}
Z	Proximal landing zone of the stent-graft	

Greek Letters

$\mathrm{\alpha}$	Womersley parameter	
γ	Ratio between diameters	
Γ	Boundary	
μ	Dynamic viscosity	Pa.s
ρ	Density	kg.m^3
τ	Wall shear stress	Pa
T	Period	s
υ	Kinematic viscosity	m^2.s^{-1}
ω	Cardiac frequency	s^{-1}
Ω	Domain	

Indexes

c	Critical value
F	Fluid
i	Outlet of the model
$inlet$	Value at the inlet
n	Number of the landing zone of the stent-graft
t	Value at the downstream vasculature
w	Value at the wall

List of Acronyms

3D	Three-dimensional
3-EWM	3-Element Windkessel Model
CFD	Computational Fluid Dynamics
CT	Computed Tomography
EVAR	Endovascular Aortic Repair
FEM	Finite Element Method
FRZ	Flow Recirculation Zone(s)
FSI	Fluid-Structure Interaction
FVM	Finite Volume Method
IA	Innominate Artery
LCCA	Left Common Carotid Artery
LSCA	Left Subclavian Artery
MRI	Magnetic Resonance Imaging
PC-MRI	Phase-Contrast Magnetic Resonance Imaging
TAWSS	Time-Averaged Wall Shear Stress
WHO	World Health Organization
WSS	Wall Shear Stress

1 Introduction

1.1 Motivation

As a response to the interaction between blood flow and arteries walls, blood vessels are able to remodel themselves over time, responding to the haemodynamic stresses they are facing. Vascular pathologies may appear as a biological response to the fluid mechanical environment.

According to the World Health Organization, WHO, cardiovascular diseases are the number one cause of death in the world, having caused 17.5 million deaths, in 2012 [1]. The most common pathologies of the aortic arch include aneurysm and dissection caused by the over time weakening of the aortic wall [2]. These vascular pathologies are associated with high risk of vessel's rupture, underlying the need for emergency surgery in such cases.

The conventional procedure for aortic arch repair is open surgery, which has a reported 7 – 17 % mortality rate [3]. In the last decade, endovascular aortic repair, EVAR, has appeared as a successful less invasive surgical procedure, consisting in the introduction of a stent-graft through an exposed access artery. The device is conducted to the desired landing site, where it is fixated, excluding the aneurysm sac or the dissection's false lumen from the mainstream blood circulation. Although EVAR for the descending aorta has acceptable rates of mid-term mortality and morbidity, EVAR for the aortic arch is still in development, owning to the challenges that this anatomical location represents.

The site's complex geometry, with extensive curvature and the presence of the three supra-aortic vessels (the brachiocephalic trunk or innominate artery, the left common carotid artery and the left subclavian artery), makes it hard to obtain a landing zone of sufficient length for the stent-graft implementation. The particular haemodynamic of this anatomical region, due to both its angulated morphology and proximity to the heart, must be carefully studied in order to accurately access the device performance.

Although there are several options when choosing a stent-graft for aortic arch EVAR, in this work branched stent-grafts were selected. Branched stent-grafts consist of a main body stent-graft with fixed branches of specific dimensions that can be oriented into the vessels of the aortic arch, making them adaptable to a wide variety of anatomical geometries. The use of this type of devices is usually associated with hybrid repair, combining aortic arch bypass with stent-grafting, to ensure landing zones of sufficient length and prevent migration of the device. The use of off-the-shelf branched stent-grafts is a particularly appealing option since their use preclude delays associated with customization of the device, allowing to reduce costs and ensuring democratization of the EVAR technique.

Blood flow analysis is of major importance when addressing vascular pathologies. Several studies on the dependence of the development of vascular diseases on flow structure have suggested that different types of shear stresses can induce different responses in the endothelial cells that constitute de inner part of the arteries walls [2, 4]. Those results suggest the possibility for a correlation between the development of this lesions and the fluid mechanical environment to which the vessels are subjected. Studies on blood flow have shed significant light over its characteristics, leading to a better understanding of cardiovascular diseases and to the development of diagnosis tools and stent-grafts of improved performance.

Haemodynamic studies have been performed experimentally using both *in vitro* and *in vivo* experimental methods. In recent years, the development of Computational Fluid Dynamics, CFD, enabled the analysis of patient-specific haemodynamic through three--dimensional numerical simulations.

1.2 Research question

In this work, numerical flow studies in simplified three-dimensional models of the aortic arch, with its three upper branches, before and after the introduction of an idealized branched stent-graft are performed.

The pre-operative geometry is based on the surgically relevant aortic arch mapping reported by Finlay *et al.*, in 2012 [5]. The idealized branched stent-graft is also based on the prototype suggested by Finlay's group [5]. As it is constructed based on the most frequent dimensions for the aortic arch, this hypothetical off-the-shell prototype stent-graft is expected to obviate the need for customization in 60 to 75 % of the cases, democratizing the use of this technique. Such results will allow to overcome one of the main disadvantages of the EVAR procedure: the delay on the device's production along with the high costs associated with its customization [4].

In this work, a new and easy to implement methodology for a resistance type outflow boundary condition is also tested. This methodology consists in the attachment of a constriction tube to the outlets of the model, imposing the resistance of the downstream vasculature.

1.3 Objectives

It is the aim of this work to analyse the blood flow in simplified three-dimensional models of the aortic arch, with its three upper branches, before and after the introduction of an idealized branched stent-graft, using CFD software. Along with the blood flow analysis, a new and easy to implement methodology for a resistance type outflow boundary condition is studied. The optimisation of the stent-graft design for the best haemodynamic performance is also assessed.

1.4 Thesis layout

This thesis begins with this introductory chapter, where a general perspective of the motivation and research questions underlying this work are presented.

Chapter 2 provides more detailed information on the aortic arch, the aortic arch pathologies and repair procedures for these diseases, highlighting the advantages associated with endovascular procedures using branched stent-grafts. An introduction to the use of Computational Fluid Dynamics in blood flow analysis, together with a review of the literature existing on this subject can also be found in this section.

The methodology employed in this work is presented in Chapter 3, where the construction of the models, as well as the mathematical and numerical flow modelling, from pre- to post-processing, are described.

In Chapter 4, the results from the numerical simulations are presented, followed by their discussion, dividing the work in two parts: the evaluation of the resistance type outflow boundary condition and the analysis of blood flow in the branched stent-grafts.

In the final chapter, the main conclusions, along with comments on the limitations of this work and suggestions for future ones are presented.

2 State-of-the-Art

2.1 The aortic arch

The aorta is the main trunk of the vascular system, conveying oxygenated blood to the tissues of the body. It begins at the upper part of the left ventricle, with a diameter of approximately 3 cm, passing upwards and to the right for about 5 cm, arching backwards and to the left, over the root of the left lung, then descending within the thorax, and entering the abdominal cavity, presenting a diameter of about 1.75 cm [6]. It is usual to divide the aorta in three sections: the ascending, the arch, and descending, which is differentiated in the thoracic and the abdominal parts [6]. The focus of this work is on the aortic arch.

The ascending aorta is about 5 cm long, beginning at the base of the left ventricle [6]. As the ascending aorta continues into the aortic arch, the calibre of the vessels is slightly increased, due to a bulging of its right wall, causing a dilatation named the bulb of the aorta [6]. On transverse section at this level, the vessel presents an approximately oval outline.

The aortic arch begins at the level of the upper border of the second right sternocostal articulation, and runs first upwards, then backwards and to the left side of the trachea, passing downwards on the left side of the body, continuing into the descending aorta [6]. The arch has two curvatures, one with its convexity upward, the other forward and to the left.

Three vessels arise from the upper part of the arch, supplying blood to the brain and upper parts of the body: the brachiocephalic trunk (innominate artery), the left common carotid artery and the left subclavian artery [6, 7]. A schematic representation of the heart with its main vessels, giving specific focus on the aortic arch and on the three supra-aortic vessels is shown in Figure 1.

The brachiocephalic trunk or innominate artery, IA, is the largest of the three supra--aortic vessels, with a length of 4 - 5 cm [6]. It arises from the convexity of the arch, and divides itself into the right common carotid and right subclavian arteries at the level of the upper border of the right sternoclavicular [6]. The principal arteries of the head and neck are the two common carotids. The left common carotid artery, LCCA, springs from the higher part of the aortic arch, behind and to the left of the IA, ascending to the level of the left sternoclavicular joint [6]. Behind it is related to the left subclavian artery, LSCA, ascending to the root of the neck and then arching laterally [6].

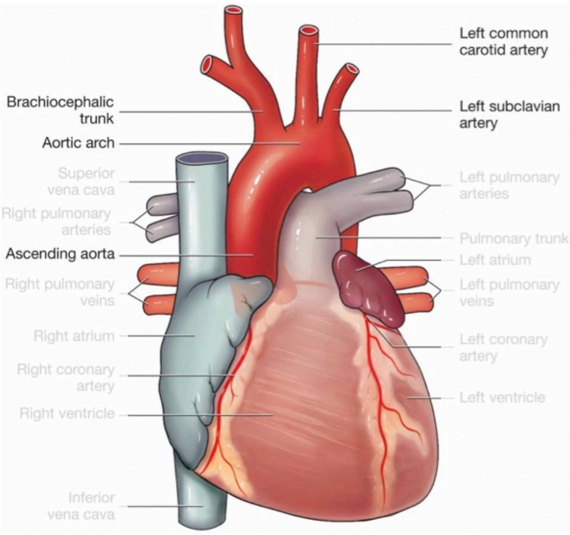
Left common carotid artery
Brachiocephalic trunk
Left subclavian artery
Aortic arch
Superior vena cava
Left pulmonary arteries
Right pulmonary arteries
Pulmonary trunk
Ascending aorta
Left atrium
Right pulmonary veins
Left pulmonary veins
Right atrium
Left coronary artery
Right coronary artery
Right ventricle
Left ventricle
Inferior vena cava

Figure 1 – The heart and its main vessels, with focus on the ascending aorta, the aortic arch, the brachiocephalic trunk or innominate artery, IA, the left common carotid, LCCA, and the left subclavian artery, LSCA.

As a response to the interaction between the blood flow and their walls, the arteries are able to remodel themselves over time, alteration that can lead to the development of diseases. The walls of the aorta consist of three thick, muscular and elastic layers: the tunica intima, tunica media and tunica adventitia, counting from the lumen [7]. Wall shear stress, WSS, has been reported as being intrinsically related to aortic pathologies [2, 7-9], with the biggest impact being seen on the intima layer that incorporates the endothelial cells in direct contact with blood.

Common diseases of the aortic arch include aneurysm and dissection. Aneurysms are local enlargements of the artery, causing thinning of the vessels wall [9]. The development of an aneurysm increases the risk of aortic dissection, which consists in the tear of the intima layer, causing blood to pass through this separation of layers of the aortic wall, producing a false lumen [10, 11]. The weakening of the aortic wall that occurs in this pathologies can lead to aortic rupture within minutes or hours of the acute event, after which the patient's risk of death increases 1 % per hour [12]. This imminent risk of rupture underlies the necessity of emergency surgery in aortic arch pathologies.

2.2 Endovascular repair of the aortic arch

The conventional procedure for the treatment of aortic arch pathologies is open surgery, which has a reported 7 - 17 % mortality rate and a 4 – 12 % neurological injury rate [3]. In the last decade, endovascular aortic repair, EVAR, appeared as a successful less invasive technique, consisting in the introduction of a stent-graft through an exposed access artery, excluding the aneurysm sac or the dissection's false lumen from the mainstream blood circulation. Although EVAR has acceptable rates of mid-term mortality for the descending aorta, EVAR for the aortic arch is less developed due to the challenges that this anatomical site represents [3, 13].

A particularly important feature of EVAR techniques using stent-graft is the need for a sufficiently long length of healthy aorta to use as the landing site, with, according to Ishimaru *et al.* [13], at least 15 mm from an arch vessel to the margin of aneurysm being required. However, in the aortic arch, the curvature and proximity of the entrance of the three vessels (IA, LCCA and LSCA) makes it difficult to obtain a landing zone with sufficient length to ensure firm fixation of the device [13].

The need to maintain blood flow to the brain and upper extremities of the body must be assessed as well, and several alternatives to assure cerebral perfusion have been reported. Some of the currently available options for EVAR of the aortic arch include (I) hybrid repair – combining aortic arch bypass with stent-grafting, and the use of (II) branched or (III) fenestrated stent-grafts.

When considering EVAR that requires aortic arch landing, techniques are usually classified according to the proximal landing zone, Z, as proposed by Balm *et al.*: $Z3$ if landing is possible in the distal arch, $Z2$ if only LSCA is occluded by the stent-graft, $Z1$ if both LCCA and LSCA are occluded and $Z0$ if all three supra-aortic vessels are occluded (Figure 2) [14].

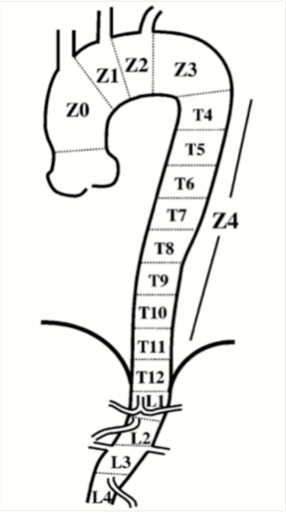

Figure 2 - Anatomical landing zone map [13].

With aortic arch repair, at least $Z2$ landing is usually required, thus a bypass of the LSCA through the LCCA to ensure blood perfusion to the upper left side of the body is essential, since the entrance of the LSCA in the aortic arch will be occluded [14]. Hybrid procedures combine the use of endovascular devices with bypass for revascularization of the cervical vessels occluded by the stent-graft, being a less invasive technique than open surgery, with promising early- and long-term results. In 2014, Shirakawa *et al.* [3] reported on the efficacy and short-term results of combined supra-aortic bypass and stent-graft into the ascending aorta for 40 high-risk patients with aortic arch pathologies. The group achieved a 3 % 30-day mortality rate and 0 % incidence of stroke occurrence, with 85 % of the patients being able to recover at home and return to independent lifestyles. Hybrid techniques are an appealing option for high-risk patients since the aortic arch bypass creates a proximal landing zone of adequate length for stent-graft deployment, preventing migration of the device.

EVAR for the aortic arch using branched stent-graft (Figure 3.A) was first reported by Inoue *et al.*, in 1997 [15], and later by Chuter and colleagues [16]. This type of devices consists of a main body stent-graft with fixed branches of specific dimensions that can be oriented into the arch's vessels. Such characteristic makes them adaptable to a wide variety of anatomical geometries.

On their turn, fenestrated stent-grafts (Figure 3.B) are customized devices in which fenestrations in the main body are aligned with the entrance of the supra-aortic vessels and secured to these by covered stents [17]. These fenestrations will house supplemental stent-grafts that protrude into the supra-aortic vessels. As these devices need to be tailor-made to ensure that the fenestrations are correctly aligned with the vessels, they require several weeks in the manufacturing, rendering their use expensive and unsuitable for urgent cases [4, 5, 17]. As mentioned by Finlay *et al.* [5], off-the-shelf branched stent-grafts would preclude this delay and reduce costs, ensuring democratization of the EVAR technique.

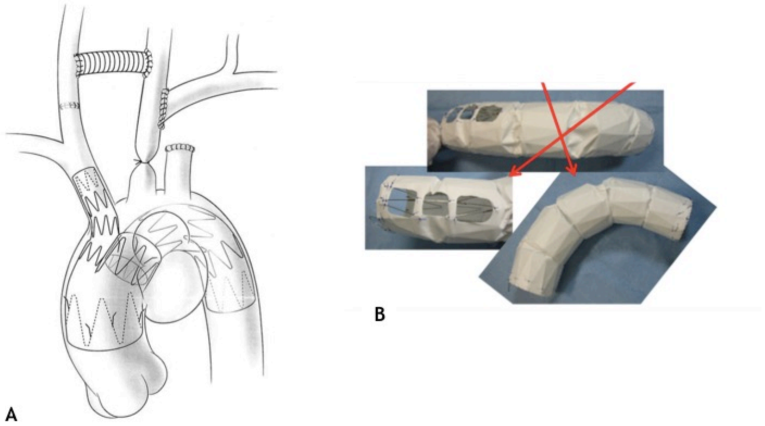

Figure 3 – (A) Schematic representation of a aortic arch branched stent-graft with a branch for the innominate artery and occlusion of both the left common carotid and left subclavian arteries [16]. (B) Precurved fenestrated stent-graft for the aortic arch with fenestration for the three supra-aortic vessels [18].

In 2012, Finlay *et al.* [5], performed a surgically relevant aortic arch mapping using Computed Tomography, CT, scans. After mapping the aortic arch diameters, branch orientations and centre line distances, the group proposed a prototype for a standard off-the-shelf stent-graft (Figure 4) that would obviate the need for customization in 60 to 75 % of cases, since its dimensions were based on the most common values obtained in CT scans [5].

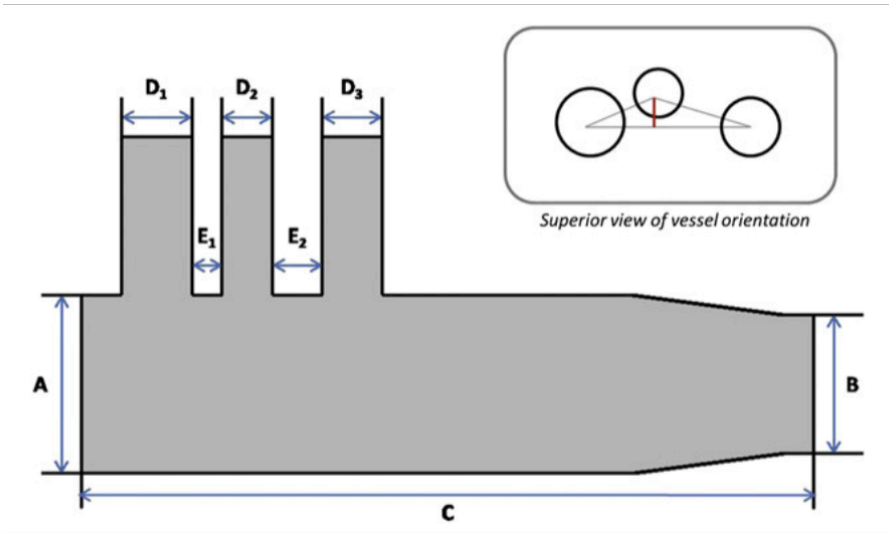

Figure 4 – Schematic drawing of the stent-graft prototype suggested by Finlay et al. [5]. A to E_2: geometric parameters based on frequency measurements of the aortic arch mapping.

2.3 Modelling blood flow using Computational Fluid Dynamics

Studies on blood flow have shed significant light over its haemodynamic characteristics, leading to a better understanding of cardiovascular diseases and to the development of diagnosis tools and stent-grafts of improved performance.

Haemodynamic studies have been performed experimentally since the 1960s using both *in vitro* and *in vivo* methods. In recent years, the development of Computational Fluid Dynamics, CFD, enabled the analysis of patient-specific haemodynamic through three-dimensional, 3D, numerical simulations. CFD simulations allow for the quantification of variables not measurable *in vivo*, and are appropriate for a combination with image-based measurements data [19]. CFD studies can be divided into four steps: problem identification, pre-processing, solving and post-processing.

2.3.1 Problem Identification

Vascular lesions tend to develop in regions of complex vessel geometry, as it is the case of the aortic arch. Several authors have used CFD simulations to study the haemodynamic in this particular region [19-23]. In fact, the curvature and non-planarity of the arch, together with the tapering of the aorta from its ascending to descending portions, have been reported as responsible for the helical patterns and flow recirculations observed there [19-23].

2.3.2 Pre-processing

The first step when carrying out blood flow simulations is to define the geometry of the region under study. Simulations can be performed in idealized or image-based patient-specified geometries.

Experimental and computational studies, conducted using both straight and curved tubes, provided a keen understanding on the influence of the arch's curvature, documenting the skewness of the velocity profiles and the appearance of secondary flow patterns. They have also provided knowledge on the influence of the non-Newtonian blood behaviour, fluid-structure interaction, mass transport phenomena, Reynolds and Dean dimensionless numbers, and Womersley parameter [19-21, 23]. The most common simplifications considered, when using idealized geometries for the aortic arch, include the assumption of circular cross-section of constant diameter, and negligence of both the curvature of the arch and the presence of the supra-aortic vessels.

Providing a realistic description of the anatomical region, image-based patient-specific geometries acquired *via* Magnetic Resonance Imaging, MRI, or CT scans have gain great popularity in the recent years. Using CT scans, high spatial resolution X-ray images are obtained with thin slice thickness and high contrast, allowing the distinct observation of different body parts through contrast adjustment. Nevertheless, CT scans are related to a certain degree of radiation, while the MRI technique, where contrast is achieved by exploiting differences in the magnetic spin relaxation properties of the body tissues and fluids using blood as the contrast agent, is thought to be benign [7, 19]. After image acquisition, it is necessary to reconstruct the geometry as a 3D model.

Once the 3D model is created, it is discretized into a mesh of finite number of smaller sub-domains over which the governing equations are solved. The smaller the number and distribution of these elements, the more accurate the simulation will be, at expense of computational costs, being essential the optimization of the ratio between solution accuracy and computational resources employed.

Meshes can be structured (hexahedral) or unstructured (tetrahedral). For the curved tubes or idealized geometries aforementioned, structured meshing has been usually used, since it can be easily automated, while unstructured meshes produced by commercial meshing software are commonly used in patient-specific simulations due to its potential of effortless grid generation over complex geometries [19]. In the later approach, distributions of tetrahedral, prismatic and pyramid elements are generated using a variety of sophisticated algorithms requiring higher resolution to reach mesh independency. When the focus of the study is on wall shear stress, boundary layer mesh generation techniques with high resolution, *i.e.*, higher mesh density near the artery wall, should be employed.

It is also essential to consider the accurate properties of the materials. Blood is a non--Newtonian fluid, since its viscosity decreases with the increase of the shear-rate, *i.e.*, it is a shear-thinning fluid [7, 19]. Blood's viscosity increases with the increase of the volume percentage of red blood cells and the decrease of body temperature [19]. The presence of red blood cells, measured in terms of their percentage, haematocrocit, gives some elasticity to the blood, which can be classified as a visco-elastic fluid. Nevertheless, the majority of the CFD studies assume blood as having a Newtonian behaviour, based on the premise that the mean shear-rate in the boundary layer exceeds 100 s^{-1}, minimum value for which the viscosity is independent of the shear-rate [7]. Sustaining this assumption is the study by Fung *et al.* [24], reporting that blood viscosity has a milder impact on the shear forces acting in the vessels walls, compared to the effects of blood pressure and pressure waveforms.

The arteries are dynamic systems that adapt over time to the haemodynamic conditions to which they are subjected, in addition to expanding and relaxing throughout the cardiac cycle. The adaptation of the walls owes primarily to the long-term variations in the WSS, τ_W, sensed directly as a force onto the endothelial cells [2]. Equation 2.1 describes WSS for a Newtonian fluid, where u is the velocity, which is zero on the wall, μ the fluid's dynamic viscosity, and a the radius of the vessel. Blood pressure has also been reported as contributing for the dynamic response of the arteries, affecting primarily the cells on the tunica media layer [2].

$$\tau_W = -\mu \frac{\mathrm{d}u}{\mathrm{d}r}\bigg|_{x=a} \tag{2.1}$$

Fluid-Structure Interaction, FSI, assigns the dynamic behaviour of the elastic walls as a response to the pulsatile blood flow and pressure. Modelling FSI is currently one of the major challenges in CFD haemodynamic simulations due to its dependence on blood flow and pressure, as well as on the tissues and organs outside the vessel, requiring extensive models of the arterial system as an all. Rigid wall assumption is commonly employed in CFD simulations, although FSI provide a more accurate description of the physiology of the site under study. However, the latter requires complex numerical algorithms and patient-specific data, drastically increasing the need for computational resources.

In order to run CFD simulations and solve the governing equations it is essential to prescribe boundary conditions that match accurately clinical data.

Although the aorta is subjected to large deformations over time due to blood flow and pressures waveforms, and it is coupled with the surrounding organs and tissues, rigid, impermeable wall and no-slip conditions at the wall of the vessels are assumed in the majority of CFD studies [11, 19-29]. The effect of blood particles is also not considered as it is expected that such approximation would yield minor effects on the simulation results, according to Lam *et al.* [30].

In the human body, the majority of the studies assume laminar flow since, even in large arteries, the velocity has been reported to be low enough to yield relatively low Reynolds numbers [24, 26, 27]. Stein and Sabbah [31], in 1976, followed by Kilner *et al.* [32], in 1997, reported the flow through the aorta of a normal adult at rest as being laminar with possible disturbances, helical and disturbed flows patterns, in specific zones. The presence of abnormalities that change the widening of the blood vessel, *e.g.*, atherosclerosis, aneurysms, dissections and stenosis, cause the flow inside the lumen to vary as well [7].

The Reynolds number, Re, given by Equation 2.2, where $\bar{u}$ is the cross-sectional mean velocity of the fluid, d the vessel's diameter, ρ the density of the fluid, μ the fluid's dynamic viscosity and thus υ its kinematic viscosity, is a measure of the ratio between the inertial and viscous forces acting onto a fluid element [33].

$$\mathrm{Re} = \frac{d^2.\bar{u}^2.\rho}{d.\bar{u}.\mu} = \frac{d.\bar{u}.\rho}{\mu} = \frac{d.\bar{u}}{\upsilon} \tag{2.2}$$

For Re values smaller than the critical, $\mathrm{Re_c}$, the magnitude of the viscous forces surpasses the one of the inertial forces, and the flow is said to be laminar, while a flow for which $\mathrm{Re} > \mathrm{Re_c}$ is said to be turbulent. In the human aorta, the Re is approximately 4 000 and turbulent flow has been reported to be present when the peak Reynolds (Re at peak systole, $\widehat{\mathrm{Re}}$) is between 5 000 and 6 000 [2, 19].

Kousera *et al.* [34], in their numerical study of aortic flow stability, presented a stability diagram, in Figure 5, showing *in vivo* disturbed and undisturbed flow data depending on the $\widehat{\mathrm{Re}}$ and the Womersley parameter.

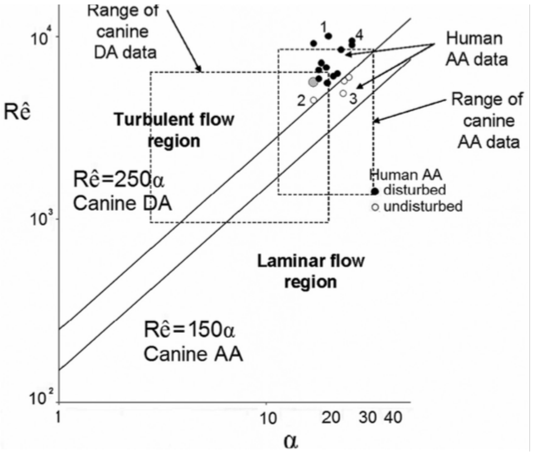

Figure 5 – Stability diagram showing in vivo disturbed and undisturbed flow data [34].

The Womersley parameter, α, is a dimensionless frequency parameter governing the relationship between the unsteady and viscous forces acting onto to the fluid element. It is mathematically described by Equation 2.3, where a is the characteristic dimension of the vessel, its radius, υ the kinematic viscosity and ω the cardiac frequency [7].

$$\alpha = a\sqrt{\frac{\omega}{\upsilon}} \tag{2.3}$$

For low α values, viscous forces dominate over unsteady ones, and velocity profile is parabolic with the centreline velocity oscillating in phase with the pressure gradient [2]. It is considered that for $\alpha > 10$ the unsteady inertial forces predominate, and the velocity profile is almost flat due to a piston-like flow motion of the flow [2].

The most common inlet boundary condition in blood flow analyses consists in prescribing an idealized velocity profile (flat, parabolic or Womersley flow pattern) together with a pulsatile waveform. In 1955, Womersley reported data on the oscillatory motion of a viscous fluid in a thin-walled elastic tube, when subjected to a pressure gradient, proposing a mathematical solution for the blood flow rate in large arteries [35]. In this work, Womersley reported fare agreement when comparing the data with determinations made using high-speed cinematography to study the motion through the translucent arterial wall [35]. Several *in vivo* studies using hot-film anemometry, such as those conducted by Seed and Wood [36], in 1971, and Nerem *et al.* [37], in 1972, have verified that the velocity profile is essentially flat in the beginning of the ascending aorta, then skews towards the inner wall in the aortic arch, with the development of a weak helical flow. The pulsatile waveform can be obtained from patient-specific MRI, Phase-Contrast MRI, PC-MRI, or CT data, or extracted from literature, being the experimental data reported by Pedley [38] the most common reference [11, 19, 20, 29, 39].

Time-varying pressure waveforms are less frequently applied as inlet boundary condition since determination of the pressure using *in vivo* catheterization techniques are extremely invasive and may induce errors by disturbing the blood flow [19].

The intensity and magnitude of the pulsatile flow and pressure waveforms generated at the heart decrease towards the capillaries. Thus, outflow boundary conditions depending on the downstream vasculature have been the focus of several studies [19]. Being impossible to trace the complete vasculature in a simulation, the model must be truncated at some point, and the downstream system must be lumped in a way that allows for an exact description of the vasculature, ensuring realistic representation of the wave propagation.

The most common CFD outlet boundary conditions for large arteries include constant or pulsatile pressures, constant/zero traction, velocity profiles, pure resistance, 3-Element Windkessel, and Structure Tree models [19, 40]. Nevertheless, some of the aforementioned do not replicate accurately the system's haemodynamic behaviour.

Since blood flow and pressure waveforms are coupled together - the pressure gradient along the arteries is the driving force of the blood flow - prescribing constant (zero) pressure at the outlet and pulsatile flow rate at the inlet seems to be a contradiction, even if the mean pressure difference between these boundaries is only a small fraction of the systolic--diastolic pulse amplitude [19]. The popularity of this technique arises from the difficulty in obtaining experimental patient-specific data on pressure, as previously mentioned, although the constant pressure approach may only be valid at the capillary level [40].

Prescribing pure resistance, assuming that pressure, p, and flow, Q, are directly proportional ($p = R.Q$, where R is the resistance), constrains p and Q to be in phase and eliminates the effect of the truncated vasculature [40].

The 3-Element Windkessel Model, 3-EWM, is a lumped model relating P and Q through a linear ordinary differential equation (Equation 2.4, where R_1 and R_2 are the proximal and distal resistances, and C the compliance), capturing the compliant and resistive effects of the vasculature, but falling short in capturing wave reflection throughout the vascular network [40].

$$\frac{\mathrm{d}p}{\mathrm{d}t} = R_1 \frac{\mathrm{d}Q}{\mathrm{d}t} + \frac{1}{R_2.C}\left((R_1 + R_2)Q - p\right) \tag{2.4}$$

The Structured Tree Model (impedance boundary condition) was developed by Olufsen [41], in 2000, and modified by Vignon-Clementel *et al.* [25], in 2006. It relates p and Q in the time domain through Equation 2.5, where k is the inverse Fourier transform of the impedance in the frequency domain, $\widehat{K}\,(x,\omega)$. Although the phase shift between p and Q is considered, the periodicity assumption, given by the period, T, is not applicable for non--periodic phenomena simulation [40].

$$p\,(x,\omega) = \frac{1}{T}\int_{-T/2}^{T/2} k\,(x,t\;-\;\xi\,).Q\,(x,\xi\,)\,\mathrm{d}\xi \tag{2.5}$$

In 2011, Pahlevan *et al.* [40] presented a new outflow model for FSI of blood flow in cardiovascular systems. In the model, the computational domain is extended through an elastic tube connected to a rigid contraction, where user-defined geometrical and material properties allow the preservation of the desired resistance, compliance, and appropriate wave reflection of a truncated vasculature. The model, Figure 6, was applied to a 3D model of the aorta and the solutions correctly captured the physiological flow behaviour.

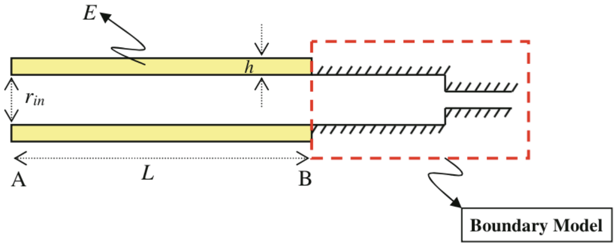

Figure 6 - Straight vessel with a rigid contraction tube [40].

For branched geometries, such as the one of the aortic arch, a widely used outlet boundary condition is to prescribe constant fractions of the inflow rate through each branch of the aorta [19, 27, 29]. This approach turns out to be unrealistic since the artery experiences considerable diameter variations throughout the cardiac cycle, as reported by van Prehn *et al.* [28], in 2007, and the assumption of constant flow through the branches states itself as inadequate. Although Pahlevan's group [40] only presented results for single outlets, they claimed that multiple outlets can be incorporated into the model by applying the outflow boundary condition from Figure 6 to each individual outlet.

2.3.3 Solving

Blood flow in the aorta is typically sufficient for blood to be assumed as an incompressible, homogenous, Newtonian fluid with a time-dependent 3D flow. The governing principles of which can be described by the conservation laws of mass (continuity equation) and momentum, *i.e.*, by the Navier-Stokes equations [24, 26, 27, 30].

The system of equations has an exact solution only for laminar flows of simple fluids. For more complex flows numerical methods implemented using CFD software are needed to solve the governing equations. Two of these methods are the finite element method, FEM, and the finite volume method, FVM.

To describe the variation of the unknown variables, the FEM makes use of approximate piecewise polynomial functions that are substituted into the governing equations. As the functions do not hold exactly during substitution, residuals are used to evaluate the errors. These errors must be minimized by multiplying them by a set of weighting function followed by integration [19]. This procedure yields a system of algebraic equations for the unknown variables.

The FVM uses an integral form of the governing equations directly into a finite number of sub-domains of smaller size – control volumes -, ensuring global conservation [19]. The terms of the integrated equation are then substituted by finite difference approximations yielding a system of algebraic equations that can be solved iteratively [19]. This methodology is valid for both structured and unstructured meshes. When using CFD software that employs FVM, attention must be taken when choosing the convergence criterion.

2.3.4 Post-processing

Once the governing equations are solved, *i.e.*, the desired convergence criterion is reached, the simulation results can be visualized and must be analysed.

For the ascending aorta and aortic arch, WSS remains the parameter most commonly studied, and has been depicted by spatial maps or trends [19]. In the case of branched geometries, studies have showed that velocity iso-contours are ideal for visualizing or quantifying the regions of flow recirculation and of retrograde flow, common patterns in these anatomical sites [19].

The results from CFD simulations must be validated in order to determine the degree to which the model exactly represents the real case under study. Validation of CFD studies requires a combination of numerical results with experimental data, and is primarily done using *in vitro* models [19]. Few cases of validation with *in vivo* data have been reported [19].

3 Methodology

3.1 Geometries

When performing CFD simulations, the first step is to select the fluid domain, Ω_F, of interest. As the focus of this work is on the aortic arch, this anatomical region was selected as Ω_F, and artificially reconstructed with the physiological dimensions reported by Finlay *et al.*, in the group's aortic arch mapping [5]. This idealized domain (Figure 7) encompasses part of the ascending aorta, the aortic arch with its three branches (innominate artery, IA, left common carotid artery, LCCA, and left subclavian artery, LSCA), and part of the descending aorta.

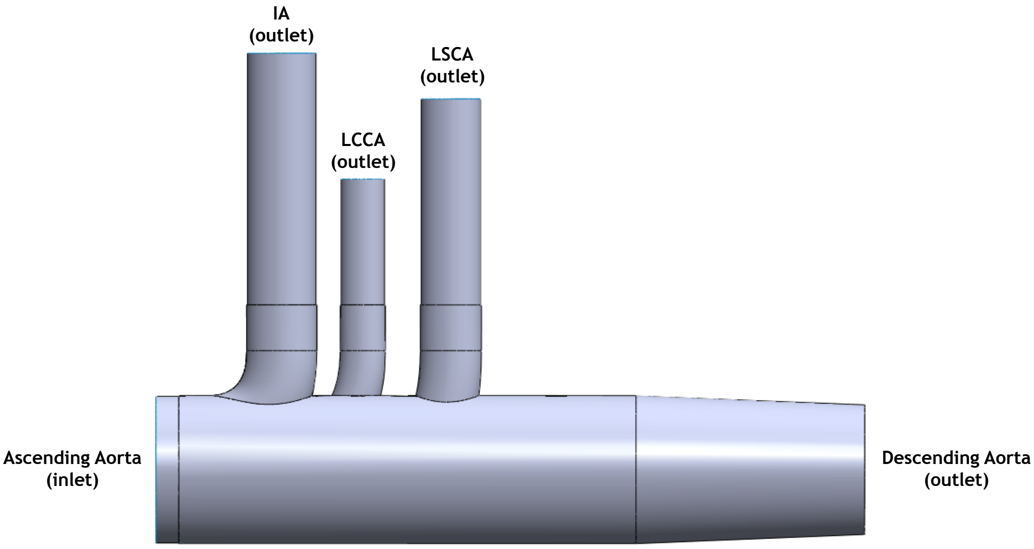

Figure 7 – Fluid domain. An artificially model of the aortic arch was selected as the fluid domain, Ω_F. The idealized geometry was reconstructed with the physiological dimensions reported by Finlay et al. [5].

Besides the geometry on Figure 7, CFD simulations were performed on three other modified geometries, which included a branched stent-graft consisting of a main body and two tunnel/branch stent-grafts for the IA and the LCCA. Such geometries were based on the prototype suggested by Finlay *et al.* [5], with the difference that, in the current work, occlusion of the LSCA and consequent bypass of this vessel through the LCCA, was considered. Such method was preferred since, for repair of aortic arch pathologies, at least $Z2$ landing (Figure 2, in Chapter 2) is usually required, thus making necessary the bypass of the LSCA through the LCCA [14]. This hybrid technique has proven itself to be an appealing option for high-risk patients since the occlusion of the vessel creates a proximal landing zone of adequate length for stent-graft deployment, preventing migration of the device.

As off-the-shelf branched stent-grafts are only manufactured in a small range of sizes, one of the aims of this work is to access the impact of the diameter of the tunnel stent-grafts for the supra-aortic vessels on the flow characteristics. This is the reason why three combinations for the diameter of the tunnel stent-grafts were tested:

- In the first geometry, the diameter of the tunnel stent-grafts matched the one of the vessels reported in the aortic arch mapping of Finlay *et al.* (15 mm for the IA, and 9.5 mm for the LCCA) – *stent-graft 1*;

- In the second (*stent-graft 2*) and third (*stent-graft 3*) geometries, the diameter of the tunnel stent-grafts was set equal to some of the most commonly manufactured diameters (8 mm and 10 mm, respectively for each geometry, for both IA and LCCA).

These new geometries are represented in Figure 8, where the difference in the diameters of the tunnel stent-grafts is made clear by the distance between their inlets, at the proximal (left) side of the models.

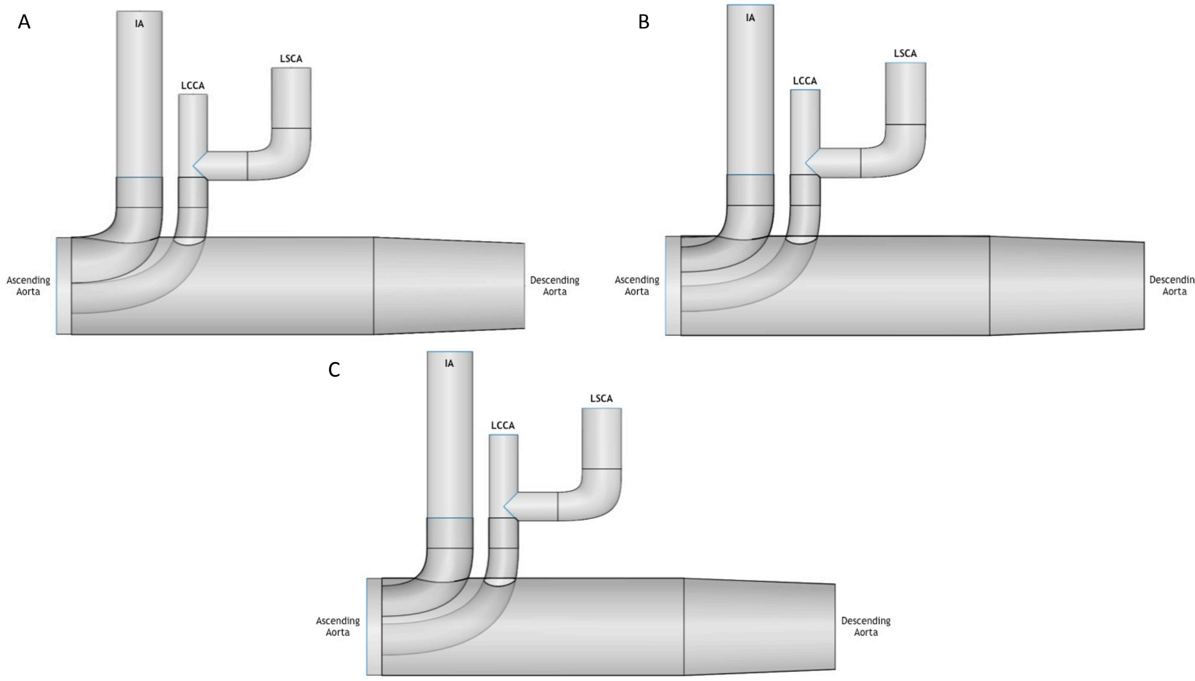

Figure 8 – Modified geometries for the fluid domain, Ω_F, including a branched stent-graft consisting of a main body and two tunnel stent-grafts for the innominate, IA, and the left common carotid, LCCA, arteries. (A) *stent-graft 1*; (B) *stent-graft 2*; (C) *stent-graft 3*.

Although the curvature and non-planarity of the arch have been reported to be responsible for helical and recirculating flow patterns observed in the anatomical region under study [19-23], neglecting the curvature is expected not to have a significant impact on the results, particularly in a preliminary approach.

The outlet length of the three supra-aortic branches was extended by five times the respective diameter, in all geometries (Figures 7 and 8), to ensure fully developed flow at their outlet, as recommended by CFD software, ANSYS CFX 15.0 (ANSYS, Canonsburg, PA, USA) [34]. Also, a cylindrical extension of arbitrarily length (5 mm) was added to the inlet to provide developed flow at the entrance of the supra-aortic vessels [17].

The dimensions of the geometric parameters used to describe the geometries can be found in Table A.1, in the Appendix.

The 3D idealized geometries were constructed using commercially available software SolidWorks 2012 (Dessault Systemes, France).

3.2 Mathematical flow modelling

In all the simulations carried out in this work, blood was considered to be a Newtonian fluid, with a density, ρ, of 1 060 kg/m^3 and a constant dynamic viscosity, μ, of 0.004 Pa.s [2, 11], feasible assumptions for large arteries such as the aorta, as it is explained in Chapter 2. Effects of the blood particles were not considered since, according to Lam *et al.* [30], they would have a minor effect on the simulation results. Flow was assumed to be laminar, common assumption in the majority of the blood flow studies, and was modelled through the Navier-Stokes equations - continuity (Equation 3.1) and momentum (Equation 3.2) conservation equations, where u represents the velocity, p the pressure and t the time.

$$\nabla . u = 0 \tag{3.1}$$

$$\rho \left(\frac{\partial u}{\partial t} + u . \nabla . u \right) = -\nabla p + \mu \nabla^2 u \tag{3.2}$$

The walls of the arteries and of the stent-graft were assumed to be solid, rigid, motionless and impermeable. For all simulations, a no-slip boundary condition was specified at the walls.

3.3 Numerical flow modelling

Besides analysing blood flow in an idealized model of a branched stent-graft for EVAR of the aortic arch, a new, and easy to implement, methodology for a resistance type outflow boundary condition is also studied in this work. Resistance type outflow boundary conditions were implemented in all four outlets of the geometries tested, using the methodology described in the following section.

3.3.1 Resistance type outflow boundary condition

Resistance type boundary conditions were imposed at the outlet boundaries, Γ_i, by attaching a rigid constriction tube (Figure 9) at every outlet. These constriction tubes were calibrated so that they can accurately offer the resistance imposed by the downstream vasculature at every Γ_i.

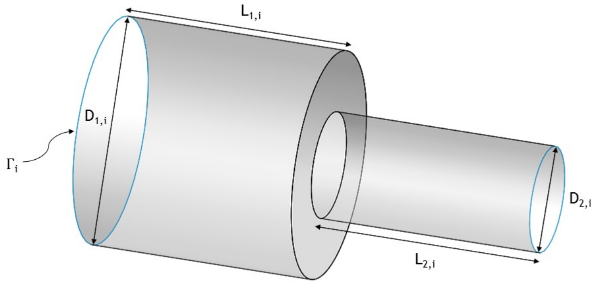

Figure 9 – Rigid constriction tube representing the resistance type outflow boundary model.

For the calibration of the constriction tubes, the first step was to determine the mean pressure values, $\bar{p}_i$, and volumetric flow rates, $\bar{Q}_i$, at the four outlets of Ω_F ($i =$ IA, LCCA, LSCA and descending aorta). This was done performing transient simulation on Ω_F from Figure 7, prescribing:

- At the inlet, a flat velocity profile combined with pulsatile flow rate waveform (Figure 10) extracted from PC-MRI data of a healthy 28 year-old male subject published by Nan Xiao [39];

- At the outlet of the three supra-aortic vessels, patient PC-MRI flow waveforms extracted from the same work (Figures 11 to 13);

- At the outlet of the descending aorta, a pressure waveform obtained by coupling the outlet with a 3-EWM, using an in-house Matlab R2015a (MathWorks, Natick, Massachusetts, USA) code. The parameters of the 3-EWM were obtained using the Nelder-Mead Simplex algorithm. Pressure was imposed to be in the physiological range, *i.e.*, between the diastolic value of 80 mmHg and the systolic peak of 120 mmHg.

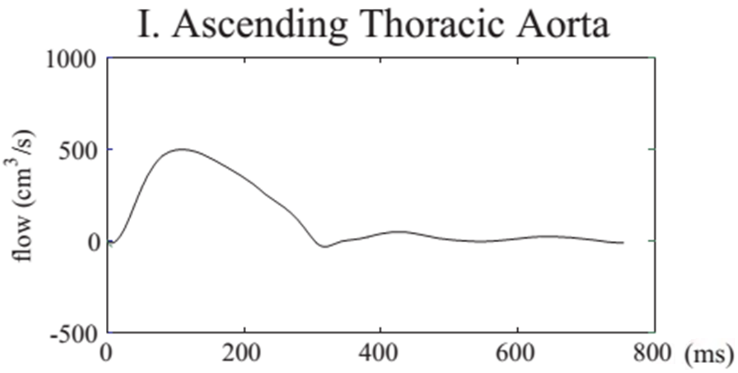

Figure 10 – Volumetric flow rate waveform at the ascending thoracic aorta. The flow waveform was extracted from Xiao [39], and corresponds to patient data acquired via Phase-Contrast MRI of a healthy 28 year-old male subject.

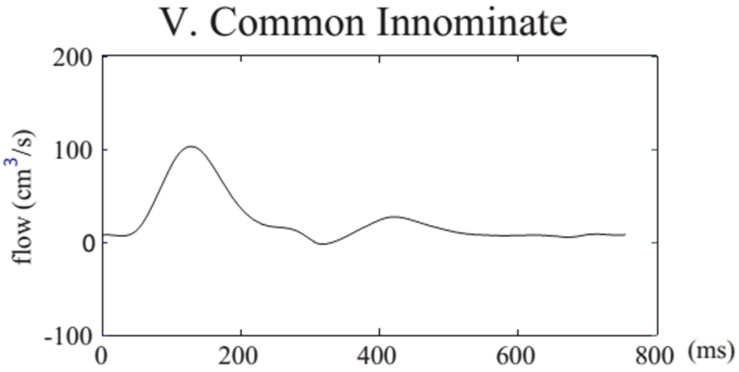

Figure 11 – Volumetric flow rate waveform at the innominate artery, IA. The flow waveform was extracted from Xiao [39], and corresponds to patient data acquired via Phase-Contrast MRI of a healthy 28 year-old male subject.

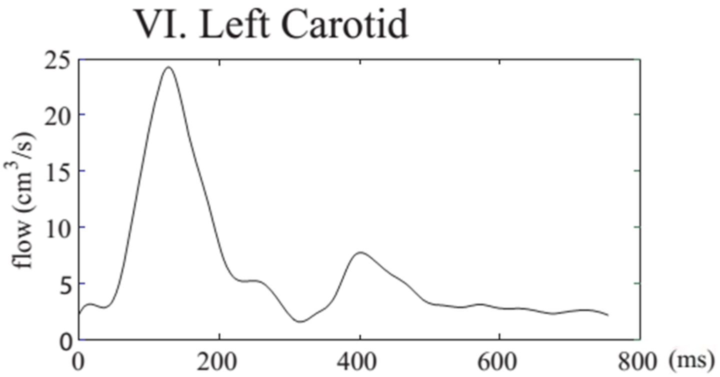

Figure 12 - Volumetric flow rate waveform at the left common carotid artery, LCCA. The flow waveform was extracted from Xiao [39], and corresponds to patient data acquired via Phase-Contrast MRI of a healthy 28 year-old male subject.

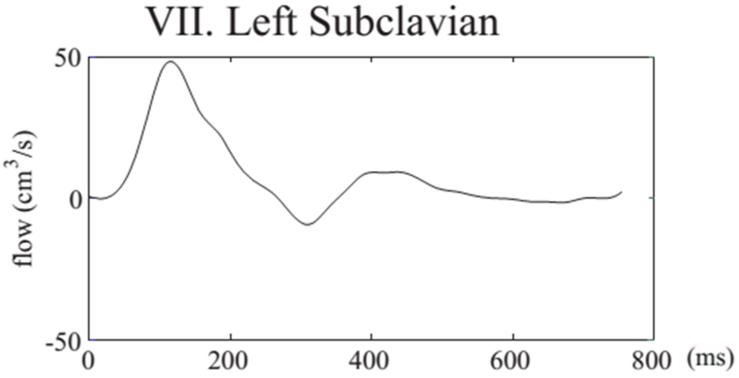

Figure 13 - Volumetric flow rate waveform at the left subclavian artery, LSCA. The flow waveform was extracted from Xiao [39], and corresponds to patient data acquired via Phase-Contrast MRI of a healthy 28 year-old male subject.

Figure 14 shows a schematic representation of the boundary conditions prescribed in this *calibration case.*

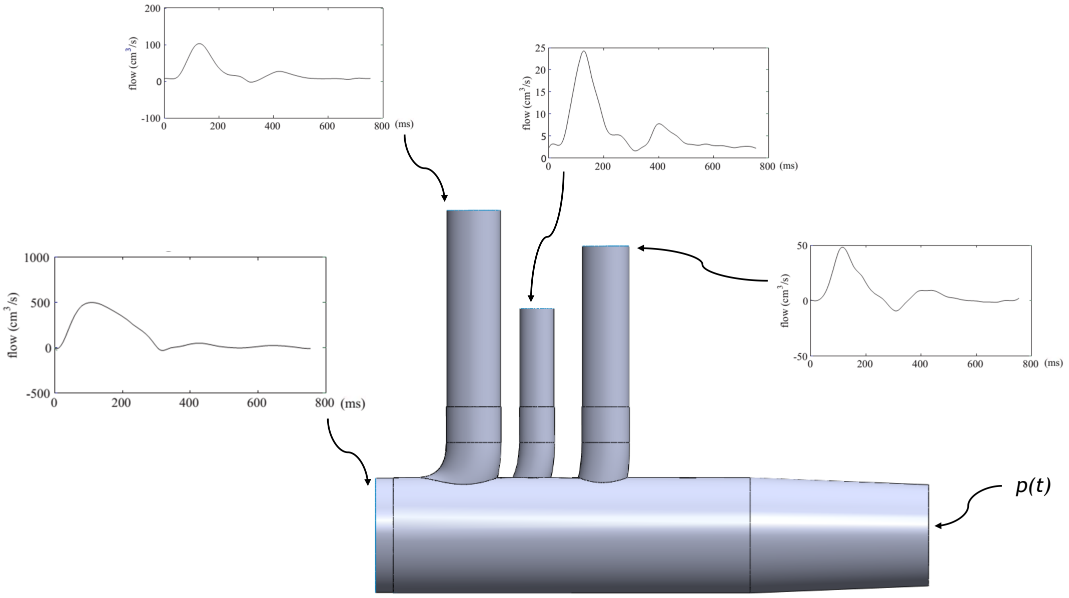

Figure 14 – Schematic of the computational model adopted in this work in order to obtain the boundary conditions for the calibration of the constriction tubes. At the inlet and outlets of the model, the boundary conditions prescribed are represented.

Four constriction tubes were constructed, one for each outlet of Ω_F. These constriction tubes constitute the outflow boundary models to be attached to the outlets of Ω_F, similarly to method described by Pahlevan *et al.* [40].

The main characteristic parameters required in order to fully define the constriction tubes are the ratio between the outlet and inlet diameters, $\gamma_i = D_{2,i}/D_{1,i}$, and the lengths $L_{1,i}$ and $L_{2,i}$, along with the pressure at the outlet of the tubes, which will correspond to the one of the downstream vasculature, $p_{t,i}$ (Figure 9). In order to represent accurately the pressure at the capillaries, $p_{t,i}$ should be as close as possible to 0 Pa. To be attached to the outlets of Ω_F, the inlet diameter of the constriction tubes, $D_{1,i}$, must be equal to the diameter of the respective outlet. $L_{1,i}$ and $L_{2,i}$ (Figure 9) were arbitrarily set equal to $D_{1,i}$.

Three steady state simulations, for different values of γ_i, were performed for each constriction tube. In these steady state simulations, the inlet and outlet boundary conditions were $\overline{p_i}$ and $\overline{Q_i}$, respectively, obtained during the transient simulations performed for calibration. As a result, the pressure at the outlet of the constriction tubes, $p_{t,i}$, was obtained.

Afterwards, the relationship between γ_i and $p_{t,i}$ (outlet pressure) was quantified as it can be seen in Figure 15, and a value of γ_i, which would yield $p_{t,i}$ sufficiently close to 0 Pa, was chosen, for the final constriction tube for each outlet. Attention should be paid to the fact that the second order polynomial trend depicted in the four charts of Figure 15 is only valid for the prescribed $\overline{p_i}$ and $\overline{Q_i}$, and should be used only in the domain presented there.

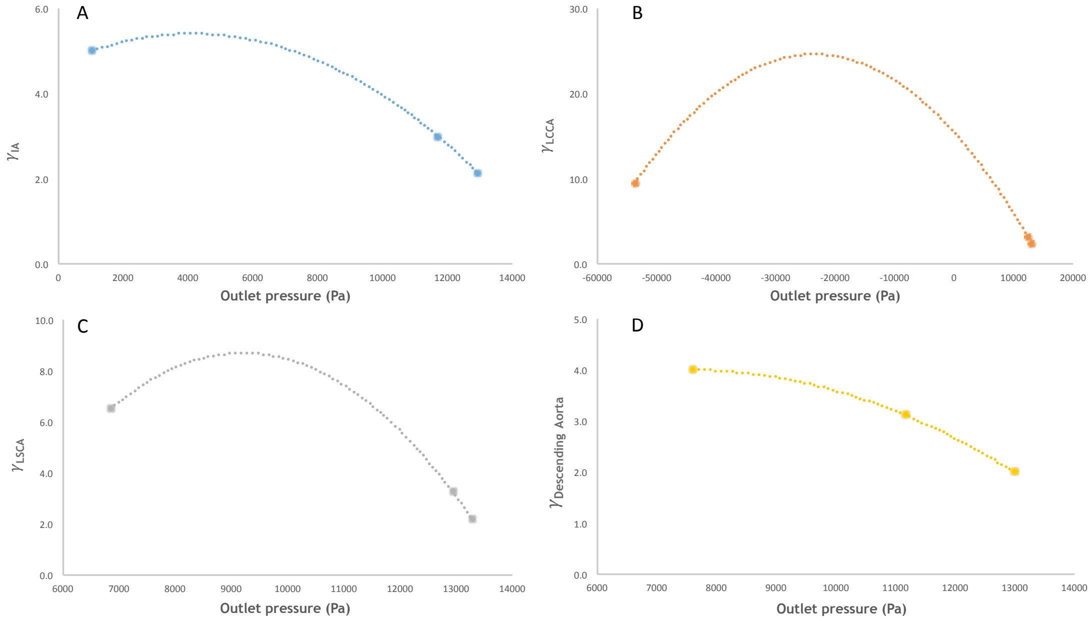

Figure 15 – Experimental relationship between the ratio of the outlet and inlet diameters, γ_i, and the outlet pressure for the constriction tubes for: (A) innominate artery, (B) left common carotid artery, (C) left subclavian artery, and (D) descending aorta. A second order polynomial trend line (dashed line) was used to establish the relationship between both variables.

After obtaining $\overline{p_\iota}$ and $\overline{Q_\iota}$ from the transient simulations performed in the calibration, and $\overline{p_\iota}$ from the steady state simulations using the constriction tubes, the resistances, R_i, at all four outlets ($i =$ IA, LCCA, LSCA and descending aorta) were quantified as:

$$R_i = \frac{\Delta p_i}{\overline{Q_\iota}} = \frac{\overline{p_\iota} - p_{t,i}}{\overline{Q_\iota}}\,. \tag{3.3}$$

These resistance values will serve as reference values on which the outflow boundary model will be built.

A constriction tube with the correct dimensions is attached to each outlet, and the respective $p_{t,i}$ is prescribed at the outlet of the constriction tube when the resistance type boundary condition is imposed. Ω_F, together with the constriction tubes attached to every outlet, constitute the fully defined CFD model, $\Omega_{F,final}$ (Figure 16).

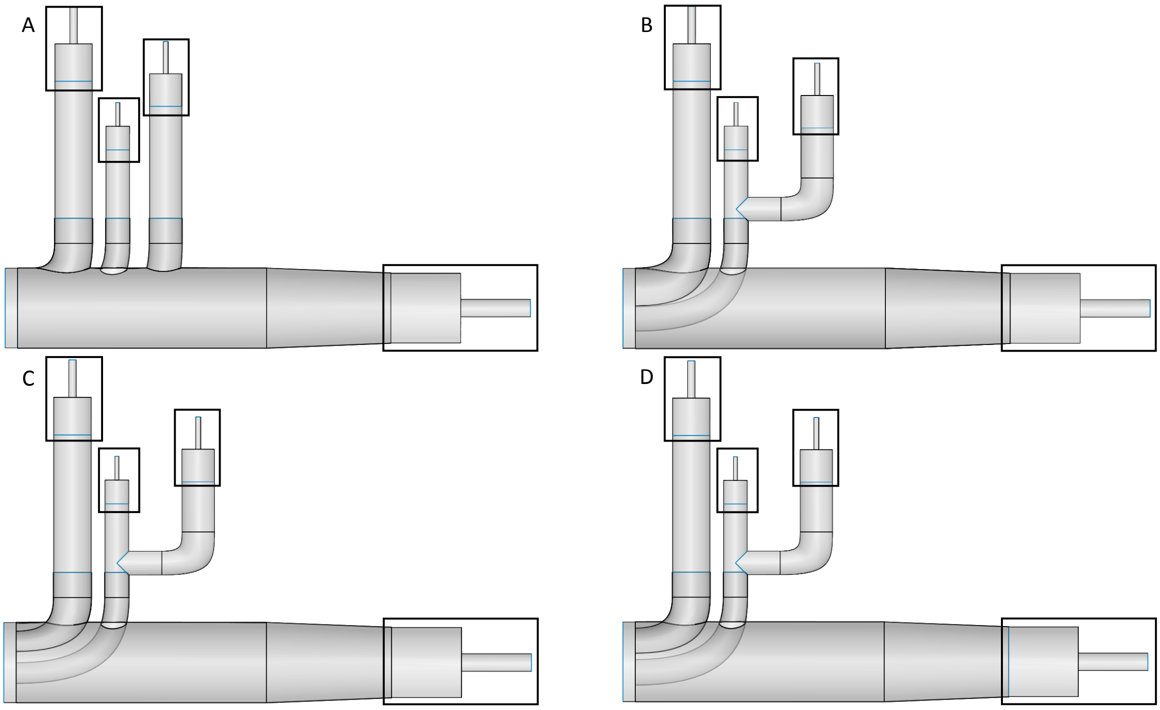

Figure 16 – Schematic of the fully defined CFD model, $\Omega_{F,final}$, for all geometries: (A) the aortic arch model, and the aortic arch model including the branched stent-graft: (B) stent-graft 1, (C) stent-graft 2, and (D) stent-graft 3.The black boxes highlight the constriction tubes.

3.3.2 Flow analysis in the branched stent-grafts

After Ω_F and $\Omega_{F,final}$ were defined, and before performing any CFD simulations, the domains were divided into a fine unstructured grid of a finite number of small volume sub--domains over which the governing Navier-Stokes equations (Equations 3.1 and 3.2) were solved. This was performed using the commercially available software ANSYS ICEM CFD 15.0 (ANSYS, Canonsburg, PA, USA). To improve the quality of the numerical results, prismatic boundary layer mesh was used along with tetrahedral elements.

Grid independence test were not carried out due to time constraints. Nevertheless, the mesh was highly refined in the curvature and in the small dimensions regions, yielding a number of elements per mesh close to or higher than one million for all geometries (Table A.2, in the Appendix).

In order to access the impact of the EVAR of the aortic arch using the branched stent--graft presented in this work, it was essential to analyse blood flow in a preoperative model of the aortic arch – *reference* case. Bearing this in mind, transient simulations were performed in the $\Omega_{F,final}$ from Figure 16.A, imposing the following boundary conditions:

- At the inlet, a flat velocity profile combined with pulsatile flow rate waveform (Figure 10) extracted from PC-MRI data of a healthy 28 year-old male subject published by Nan Xiao [39];

- At all four outlets, resistance type boundary conditions.

Despite the studies of Seed and Wood [36], in 1971, and Nerem *et al.* [37], in 1972, reporting essentially flat velocity profile in the beginning of the ascending aorta, two problems should be pointed out:

- The ascending aorta section of the models is located considerably distant from the heart root, at the end of the ascending aorta;

- It is only possible to prescribe a flat/uniform velocity profile at the inlet if there is sufficient length for the flow profile to be fully developed before reaching the entrance of the branches, which may not be true in this case, as highlighted during the description of the geometries (first section of this chapter).

To overcome this limitation and evaluate the impact of the velocity profile on the results, the previous simulation for the *reference case* was repeated, substituting the uniform velocity profile at the inlet for a Womersley velocity profile. Equation 3.4 corresponds to the mathematical expression of the Womersley velocity profile for oscillatory motion of a viscous fluid in a rigid tube, as reported by Womersley, in 1955 [35]:

$$u\,(r) = \frac{Aa^2}{\mu} \cdot \frac{1}{i^3 \alpha^2} \left\{ 1 - \frac{J_0\left(\alpha . \frac{r}{a} . i^{3/2}\right)}{J_0\left(\alpha . i^{3/2}\right)} \right\} e^{i\omega t} \tag{3.4}$$

where a is the radius of the tube, $u(r)$ the radial velocity, $Ae^{i\omega t}$ represents the pressure gradient, μ the dynamic viscosity of the liquid, and α the non-dimensional quantity known as Womersley parameter.

Finally, it was possible to performed CFD simulations in the models for the aortic arch including the branched stent-grafts (*stent-graft 1, 2* and *3* from Figure 16.B, C and D, respectively), which was done prescribing the following boundary conditions:

- At the inlet, a Womersley velocity (Equation 3.4) profile combined with pulsatile flow rate waveform (Figure 10) extracted from PC-MRI data of a healthy 28 year-old male subject published by Nan Xiao [39];

- At all four outlets, resistance type boundary conditions.

ANSYS CFX 15.0 (ANSYS, Canonsburg, PA, USA), a commercially available package, was the software used in all CFD simulations. The equations were discretised through the finite volume method, FVM.

The 3D blood flow in the aorta was assumed incompressible, homogenous and time-dependent, with Newtonian behaviour. The governing equations are derived from Newton's laws applied to fluid motion: mass and momentum conservation equations (Equations 3.1 and 3.2).

From Figure 10, it is possible to see that the peak systolic flow rate, $\hat{Q}$, prescribed at the inlet is 500 cm^3/s. Since the diameter of the inlet was the same for all geometries (Table A.1, in the Appendix), the mean inlet velocity, $\bar{u}$, at the inlet is determined by:

$$\bar{u} = \hat{Q}/S, \tag{3.5}$$

where S is the cross-sectional area at the inlet.

Considering this mean velocity, the maximum Reynolds number, $\widehat{\mathrm{Re}}$, correspondent to the peak systole value, and the Womersley parameter, α, both based on the inlet area, were determined: 5 272 and 23.7, respectively. The determination of $\widehat{\mathrm{Re}}$ and α is accessible in the Appendix. The representation of $\widehat{\mathrm{Re}}\ vs.\ \alpha$ in the stability diagram from Figure 5, in Chapter 2, places the flow in the laminar regime (Figure 17), validating the assumptions previously made.

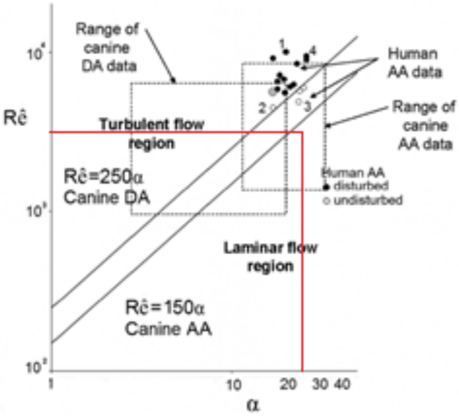

Figure 17 – Stability diagram [34]. Representing the peak systole Reynolds number, $\widehat{Re}$, against the Womersley parameter, α, determined at the inlet (intersection of the red horizontal and vertical lines) yields a point in the laminar flow region.

Transient simulations were run for two cardiac cycles of 0.76 s each. The results were then used to initialise a third cycle with the same duration. The convergence criterion based on the root mean square residues was set equal to 10^{-5} and a uniform 0.001 s time-step was used.

The post-processing of the results was performed using ANSYS CFD-Post 15.0 (ANSYS, Canonsburg, PA, USA) and EnSight 10.1 (CEI, Apex, North Carolina, USA), and will be further elaborated in the following chapter.

4 Results and Discussion

4.1 Results

Results can be divided into three categories:

(a) *Calibration case* where the calibration of the constriction tubes was performed;

(b) *Reference case* where simulations with the geometry from calibration were performed with resistance type outflow boundary conditions. Firstly imposing a uniform velocity profile at the inlet, along with a pulsatile flow rate waveform, and repeated with a Womersley velocity profile;

(c) The geometry was then modified to include a branched stent-graft for the aortic arch and a bypass of the LSCA through the LCCA. Simulations were performed for three different combinations of the diameters of the tunnel stent-grafts, prescribing Womersley velocity profile combined with a pulsatile flow rate waveform at the inlet and resistance type boundary condition at the outlets.

Key results, that will be further presented and discussed, are volumetric flow rate and pressure waveforms, specific resistance, as well as the split of blood inflow into the outlets of the models, in order to access the accuracy of the resistance type boundary condition prescribed. Time-averaged wall shear stress, TAWSS, flow patterns, particularly flow recirculation zones, FRZ, in the post-operative geometries resulting from the stent-grafting of the aortic arch, were also assessed in order to evaluate the performance of the devices.

4.1.1 *Calibration case vs. Reference case*

Volumetric flow rate waveforms prescribed in the *calibration case* and those obtained from the transient simulations for the *reference case*, at the outlet of the three supra-aortic vessels (IA, LCCA and LSCA), are shown in Figure 18. From those waveforms, the cycle--averaged percentage of flow split into the four outlets of the model (IA, LCCA, LSCA and descending aorta) was determined for both cases, and can be found in Figure 19. Comparison between the mean flow rate in the *calibration* and *reference cases* can be found in Figure 20.

It can be noted, from Figure 18, that the resistance type boundary condition captures the main flow features, following the trend observed in the original patient-specific PC-MRI flow waveforms, prescribed in the *calibration case*. The flow in the IA and LCCA is always positive, while reverse flow can be observed in the LSCA during diastole. Nevertheless, the magnitude of the flow rate decreases in the *reference case*, comparing to its real values.

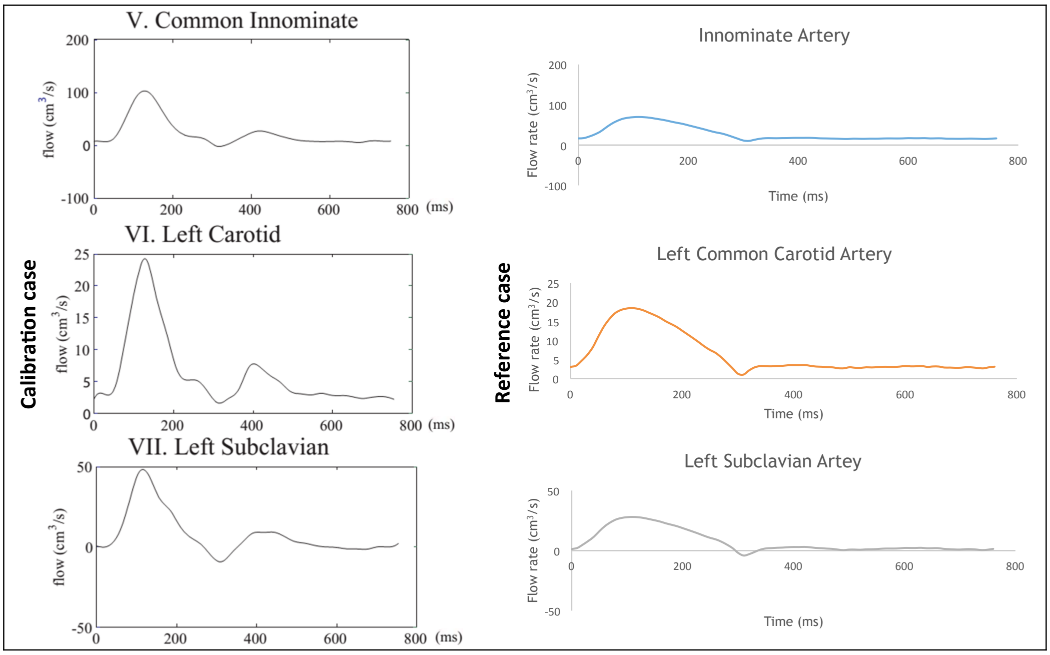

Figure 18 – Flow rate waveforms prescribe in the calibration case from patient PC-MRI data (on the left) and those obtained in the reference case (on the right), for the three supra-aortic vessels. Results are presented over one cardiac cycle (0.76 s).

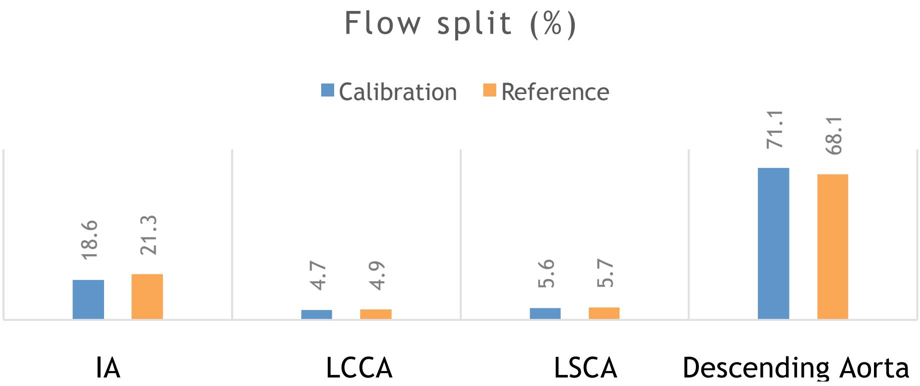

Figure 19 – Blood inflow split into the four outlets of the aortic arch model for the calibration and reference cases.

Using the resistance type boundary condition in the *reference case* yields percentages of blood inflow very similar to those in the *calibration case*. A maximum difference of 3 % is reported for the blood inflow into the descending aorta (Figure 19). The use of a resistance type boundary condition increases the percentage of flow split into the three supra-aortic vessels, particularly into the innominate artery, with a consequent decrease of the inflow into the descending aorta.

The mean flow rate in the *reference case* is 14.3 %, 3.2 % and 1.8 % higher for the IA, LCCA and LSCA, respectively, being 4.3 % lower for the descending aorta (Figure 20).

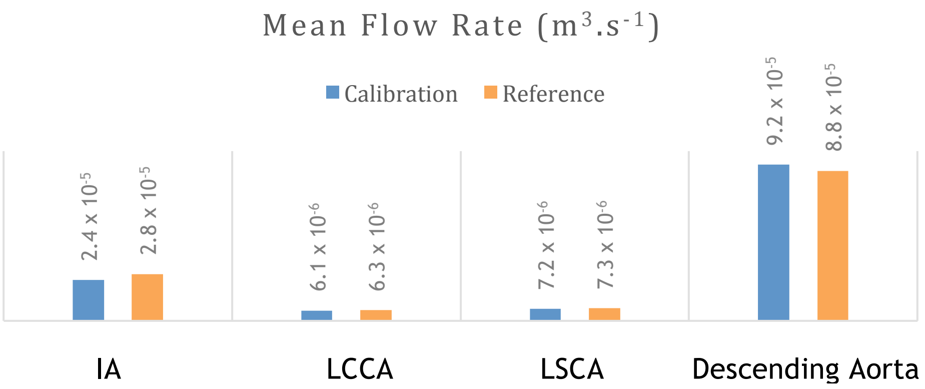

Figure 20 - Mean volumetric flow rate at the four outlets of the aortic arch model for the calibration and reference cases.

The outlet pressure waveforms obtained for the *calibration and reference cases* are shown in Figure 21, for all four outlets of the model. One significant difference between the results is the temporal dependence of the pressure waveforms. In fact, in the *reference case*, no phase lag between the flow (Figure 18) and the pressure waveforms (Figure 21) occurs. Besides, the shapes of the pressure waveforms and of the flow waveforms are very similar, expected result in line with the relationship prescribed by Equation 3.3.

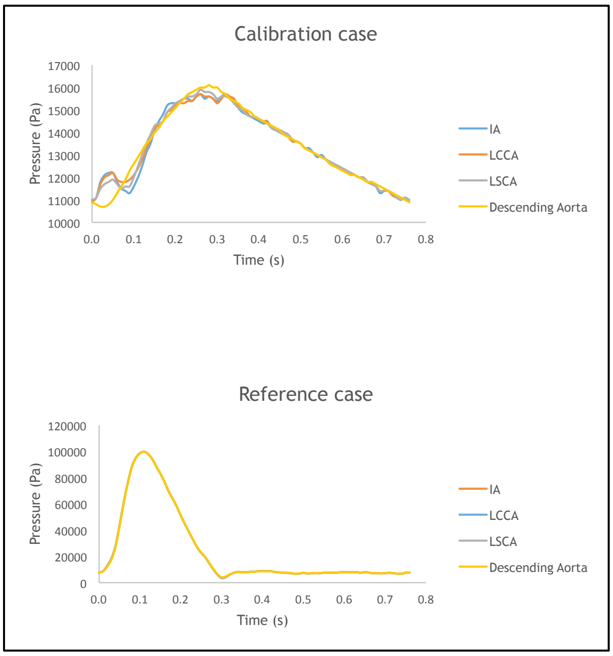

Figure 21 - Pressure waveforms at the four outlets of the aortic arch model, for the calibration and reference cases. Results are presented over a cardiac cycle (0.76 s).

4.1.2 Reference case: uniform velocity profile *vs.* Womersley velocity profile

In order to evaluate the influence of the velocity profile at the inlet, the *reference case* was repeated maintaining the resistance type boundary conditions at the four outlets, and changing the inlet boundary condition from a uniform velocity profile associated with a pulsatile flow rate waveform, to a Womersley velocity profile.

This alteration yielded no significant differences: in both cases, the flow rate waveforms exhibit the same trend and capture the physiological characteristics of the flow (Figure 22). The mean flow rate at the outlets (Figure 23) differs by a maximum of 1.6 %, value registered for the LSCA, while the blood inflow split (Figure 24) into each outlet is coincident.

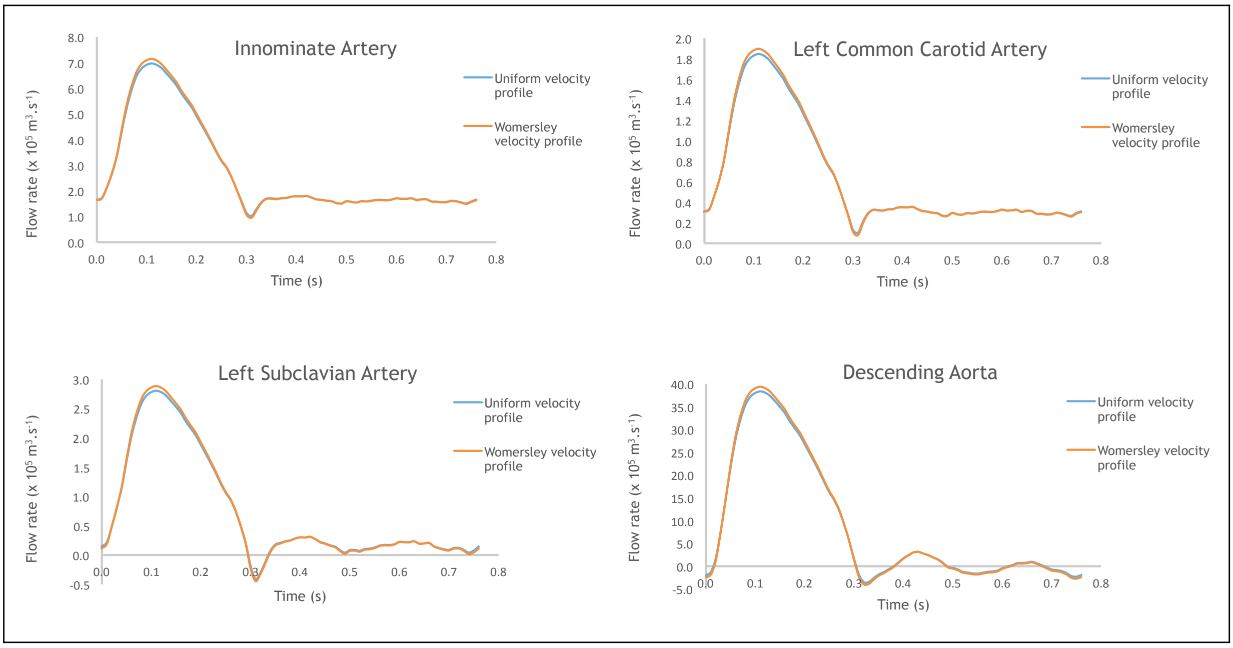

Figure 22 – Flow rate waveforms at the four outlets of the aortic arch model, for a uniform and for a Womersley velocity profiles at the inlet (*reference case*). Results are presented over a cardiac cycle (0.76 s).

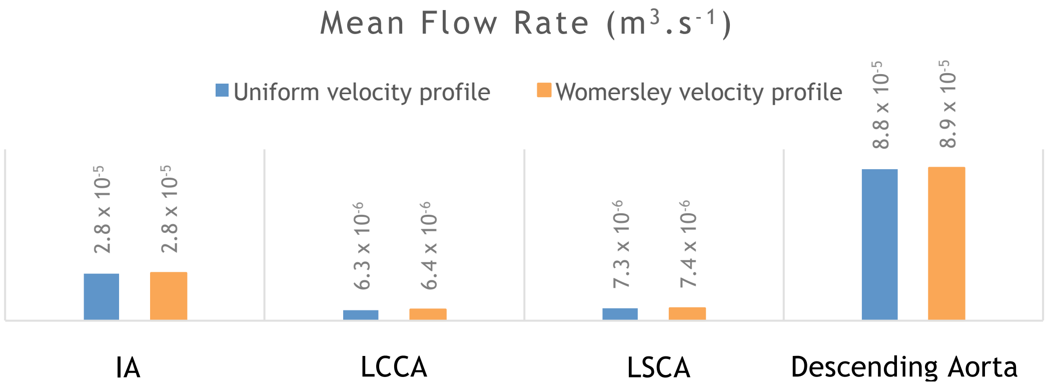

Figure 23 - Mean volumetric flow rate at the four outlets of the aortic arch model, for a uniform velocity profile and for a Womersley velocity profile at the inlet (reference case).

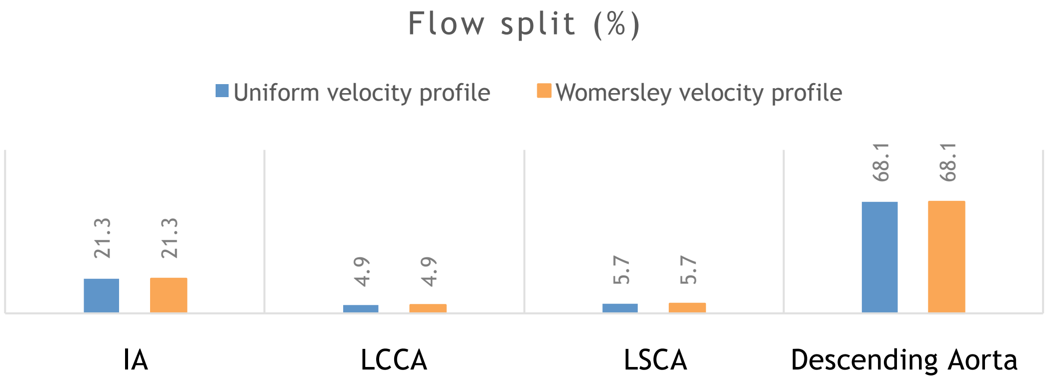

Figure 24 – Blood inflow split into the four outlets of the aortic arch model, for a uniform velocity profile and for a Womersley velocity profile at the inlet (reference case).

Specific resistances for all outlets were calculated using Equation 3.3, and identical values were obtained (Figure 25). The results suggest that the resistances, as well as the temporal flow behaviour, do not depend strongly on the velocity profile prescribed at the inlet, which may only affect the spatial flow patterns. These resistance values were used in the simulations with the modified geometries, including the branched stent-grafts.

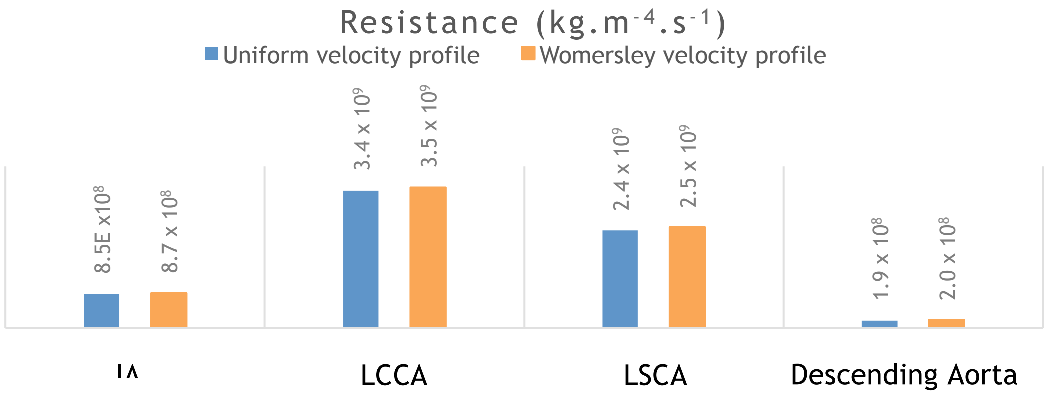

Figure 25 – Specific resistance for all outlets of the aortic arch model, for a uniform velocity profile and for a Womersley velocity profile at the inlet (reference case).

4.1.3 Branched stent-grafts for the aortic arch

The following work can be seen as a virtual scenario where the blood flow in the aortic arch of three patients treated with three different geometries branched stent-grafts is compared to the one of a healthy person (*reference case*).

Volumetric flow rate waveforms at all the outlets of the aortic arch models (one for the reference case and three for the modified geometry including the stent-graft) are shown in Figure 26. From those waveforms, the cycle-averaged percentages of flow split into the four outlets of the models (IA, LCCA, LSCA and descending aorta) were determined (Figure 27). The mean values of the volumetric flow rate at the outlets are also shown in Figure 28.

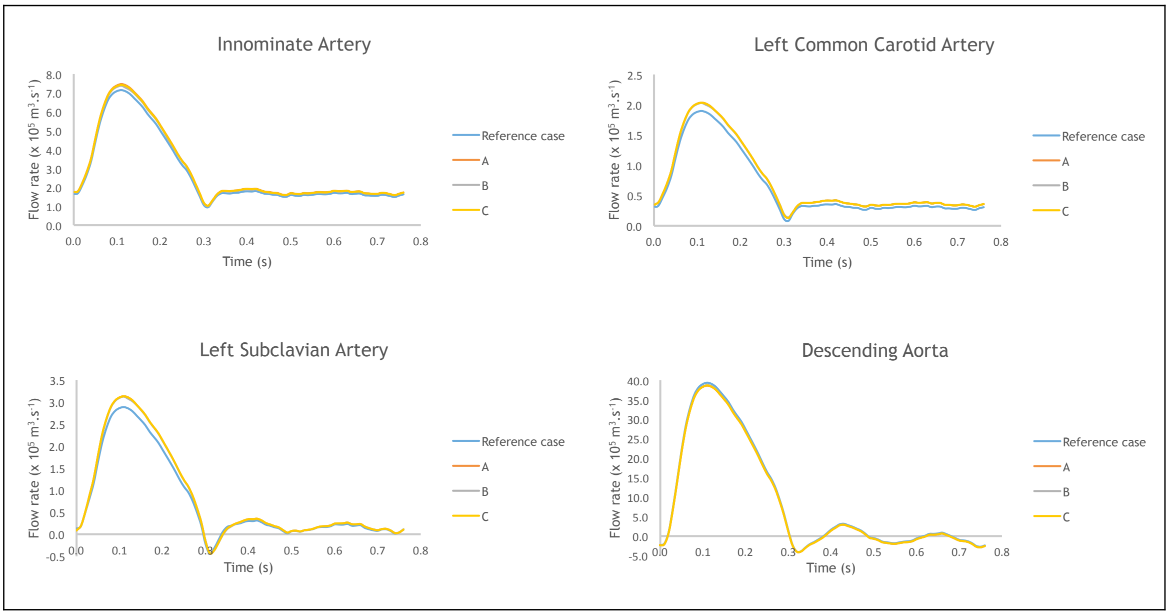

Figure 26 - Flow rate waveforms at the four outlets of the aortic arch models for the reference case and for the three geometries including a branched stent-graft: (A) stent-graft 1, (B) stent -graft 2, (C) stent-graft 3.

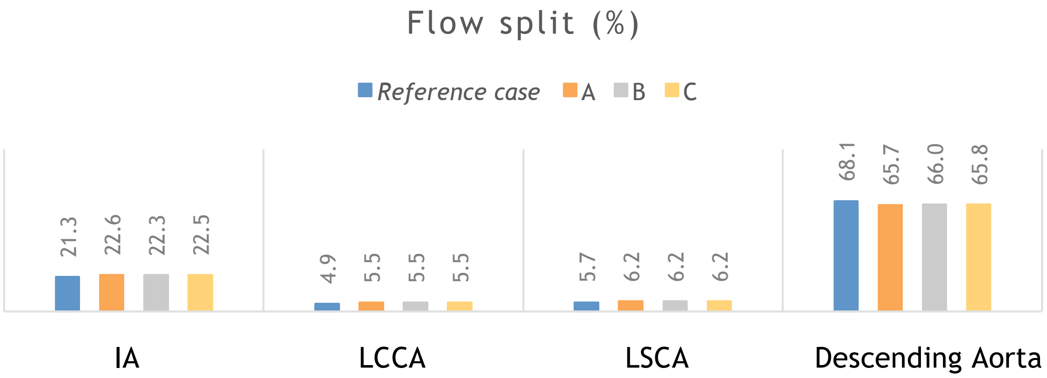

Figure 27 - Blood inflow split into the four outlets of the aortic arch models for the reference case and for the three geometries including a branched stent-graft: (A) stent-graft 1, (B) stent-graft 2, (C) stent-graft 3.

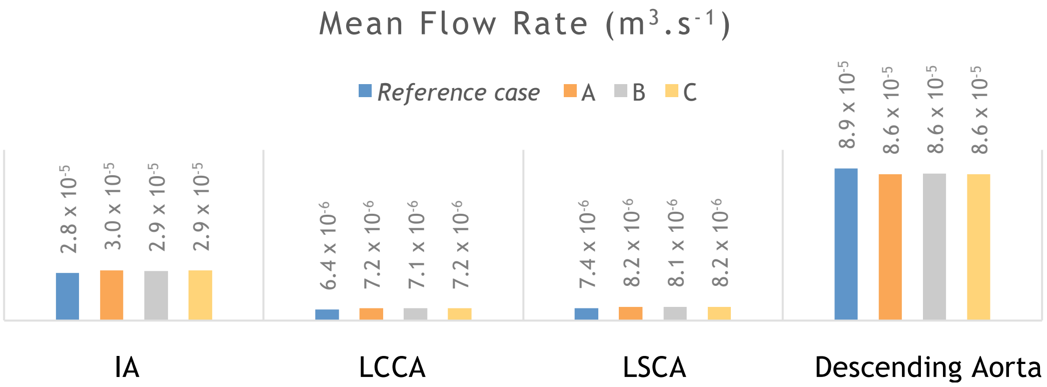

Figure 28 – Mean volumetric flow rate at the four outlets of the aortic arch models for the reference case and for the three geometries including a branched stent-graft: (A) stent-graft 1, (B) stent--graft 2, (C) stent-graft 3.

The data from Figures 26 to 28 suggest that the stent-graft increases blood perfusion through the three supra-aortic vessels (4 – 6 % for the IA, 11 % for the LCCA, and 9 % for the LSCA), and, consequently, decreases the amount of blood flowing through the descending aorta by 3 - 4 % (comparison with the *reference case*, *i.e.*, aortic arch without stent-graft). No significant differences, in the mean volumetric flow rate values at the outlets and in the blood flow split into each outlet, were found between the three stent-grafting geometries.

Specific resistances for all outlets of the models were calculated using Equation 3.3. As it can be seen in Figure 29, the specific resistances differ very slightly for all the performed simulations: only fairly lower values for the supra-aortic vessels (and higher for the descending aorta) are observed in the geometries that include the stent-graft, once again in line with the relationship prescribed by Equation 3.3, *i.e.*, for the same pressure gradient, an increase in the mean flow rate implies a decrease in the resistance value.

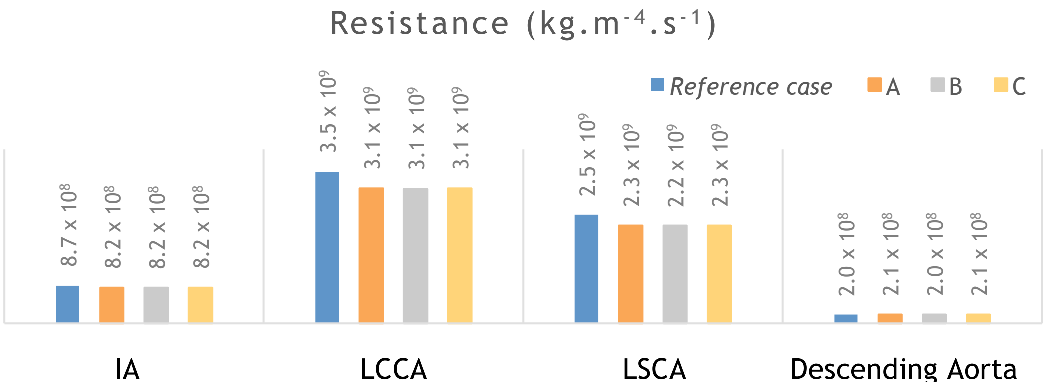

Figure 29 - Specific resistance for all outlets of the aortic arch models for the reference case and for the three geometries including a branched stent-graft: (A) stent-graft 1, (B) stent-graft 2, (C) stent--graft 3.

Time-averaged wall shear stresses, TAWSS, and flow patterns, with particular emphasis on flow recirculation zones, FRZ, in the aortic arch models, were also assessed.

The results (Figure 30) indicate that wall shear stress is higher at flow entrance regions:

- In the distal wall at the entrance of the three supra-aortic vessels - *reference case*;

- In the distal wall at the entrance of the of branches of the stent-graft, particularly in that of the IA;

- In the distal wall of the LSCA, in the bypass region, for the three post-operative geometries.

The magnitude of the TAWSS was found to be higher in the models including the stent-graft, when comparing to the *reference case* (52 – 62 %). The highest TAWSS being experienced at the walls of the model including *stent-graft 2*, branch stent-grafts with diverging tunnels (Figure 30.C). The lowest TAWSS values are for *stent-graft 3* (Figure 30.D). Regions of low TAWSS along the proximal wall of the LSCA in the bypass region are observed in all three geometries.

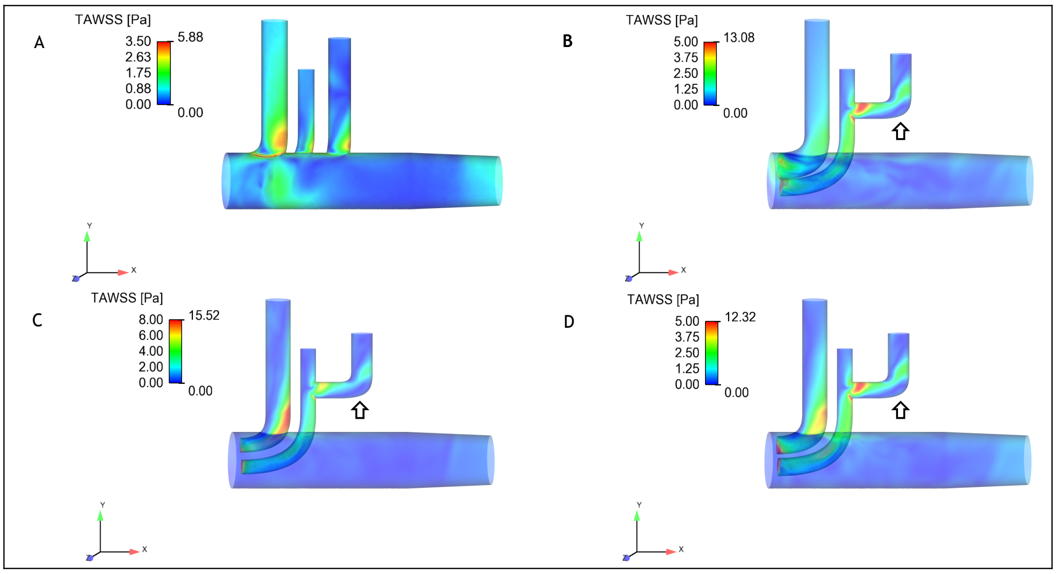

Figure 30 - Time-averaged wall shear stress, TAWSS, contours for the models of the aortic arch (A) without stent-graft, and including the branched stent-graft: (B) stent-graft 1, (C) stent-graft 2, (D) stent-graft 3. The arrows mark flow recirculation zones found in the bypass of the LSCA through the LCCA, which are regions of low TAWSS.

To evaluate instantaneous variables, such as velocity, specific time-points over the cardiac cycle must be selected. The most common ones are peak systole, diastole and the mid-deceleration time-point between the latter two (Figure 31).

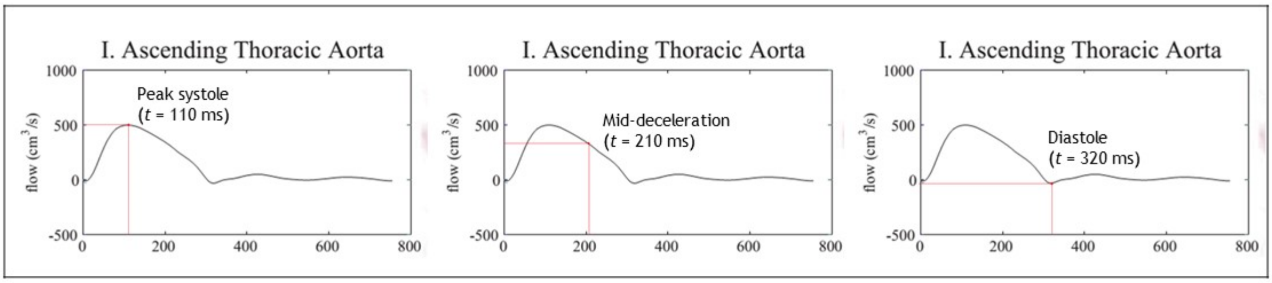

Figure 31 – Time-points over the cardiac cycle.

Flow patterns during peak systole ($t = 0.11$ s) and mid-deceleration time-point ($t = 0.21$ s) were compared by means of the instantaneous velocity streamlines at those time points (Figures 32 and 33, respectively). Disturbed flow is particularly visible in the mid--deceleration time-point, with a highly helical flow pattern visible at the aorta section right under the entrance of the IA, and throughout this vessel, in the *reference case*. The results from Figure 33 suggest that the introduction of the stent-grafts increases the region of disturbed flow in the aorta, especially in the regions downstream of the branch stent-grafts, with return of the flow to its undisturbed patterns further towards the descending section of the aorta, at the level of the LSCA.

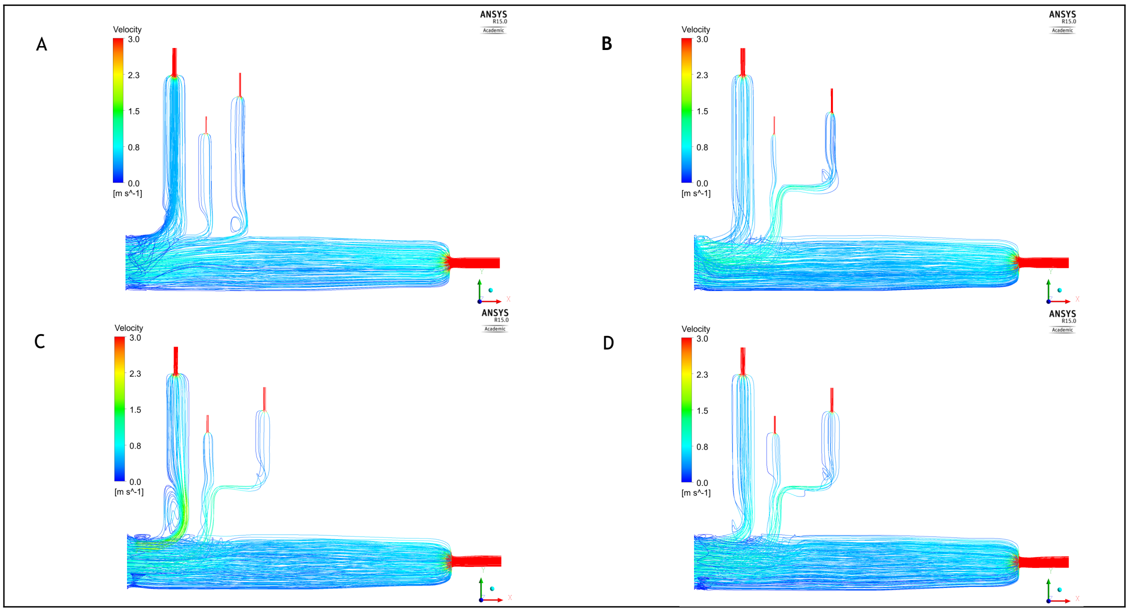

Figure 32 - Velocity streamlines during peak systole (t = 0.11 s) observed in the models of the aortic arch (A) without stent-graft, and including the branched stent-graft: (B) stent-graft 1, (C) stent-graft 2, (D) stent-graft 3.

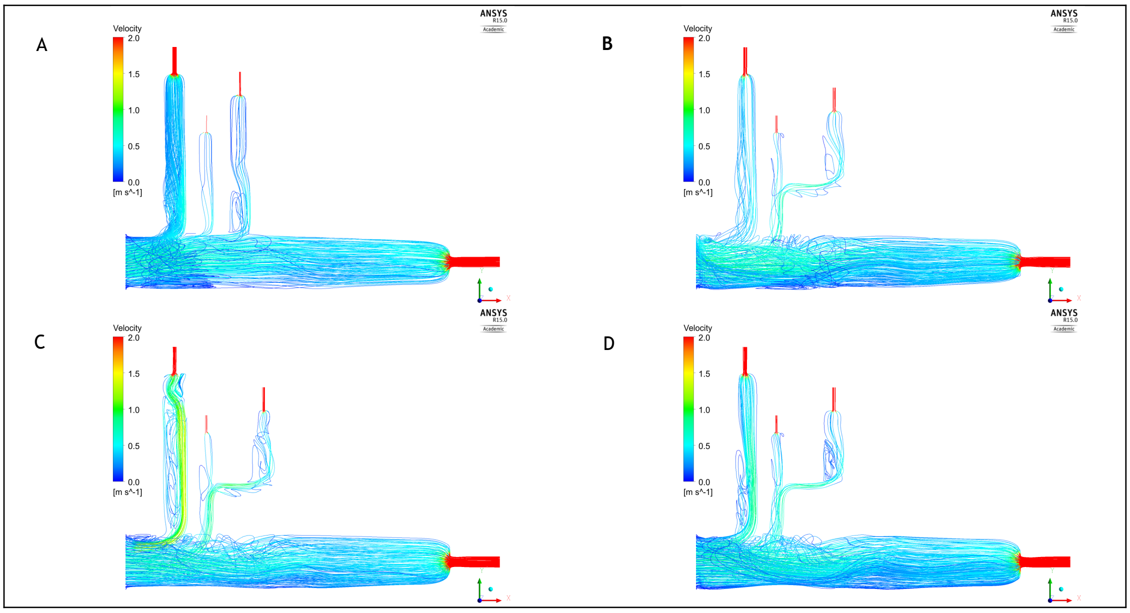

Figure 33 – Velocity streamlines during mid-deceleration time point (t = 0.21 s) observed in the models of the aortic arch (A) without stent-graft, and including the branched stent-graft: (B) stent-graft 1, (C) stent-graft 2, (D) stent-graft 3.

Flow recirculation zones, FRZ, are usually associated with low wall shear stresses, WSS, which have been reported to stimulate plaque deposition, and consequently increase the risk of thrombosis' development, as mentioned in Chapter 2. Flow recirculation zones were found in all models, at regions of sudden flow direction changes: near the proximal wall in the inlet region of the three supra-aortic vessels in the *reference case*; proximal wall in the inlet of the IA and LCCA, in the post-operative geometries; and proximal wall of the bypass region, as it is highlighted in Figure 34. To compare FRZ, the mid-deceleration time-point ($t = 0.21$ s) was chosen as it is when largest FRZ are observed.

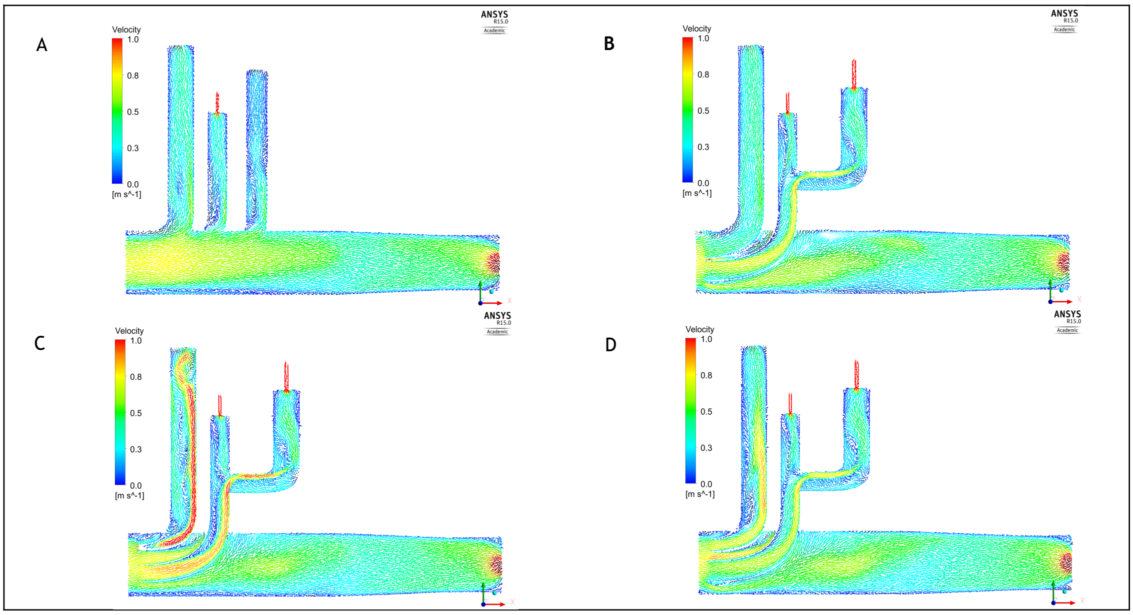

Figure 34 - Velocity vectors highlighting the flow recirculation zones, FRZ, found in the models of the aortic arch (A) without stent-graft, and including the branched stent-graft: (B) stent-graft 1, (C) stent-graft 2, (D) stent-graft 3, at $t = 0.21$ s.

The sudden change in the flow direction, from vertical to horizontal or horizontal to vertical, is the main responsible for the development of the recirculation regions in the bypass of the three models including the stent-graft.

FRZ in the bypass region were quantified by measuring the distance between the flow separation and reattachment points (Figure 35). Comparing Figures 30, 34 and 35, it is possible to see that FRZ are, in fact, regions of low TAWSS.

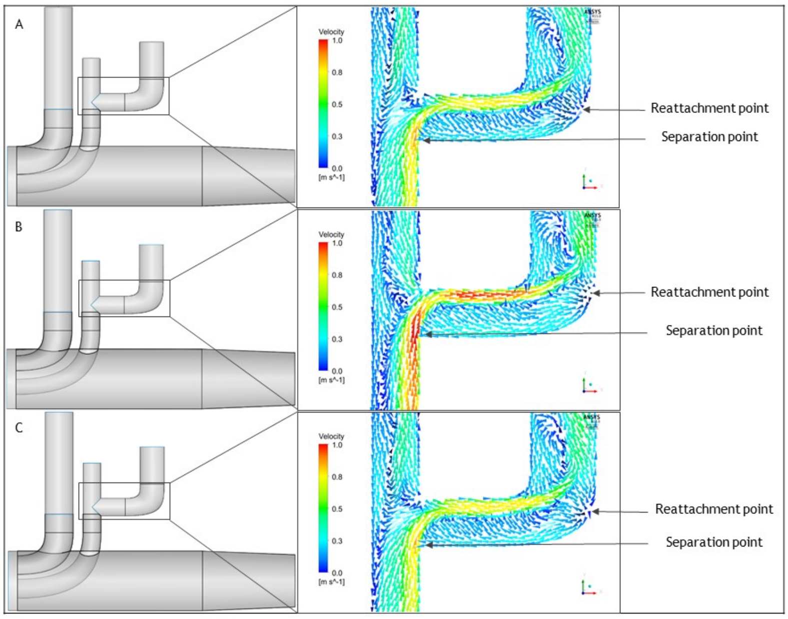

Figure 35 – Velocity vectors highlighting the separation and reattachment points of the flow recirculation zone, FRZ, at $t = 0.21$ s, in the bypass region of the three geometries including a branched stent-graft: (A) stent-graft 1, (B) stent-graft 2, (C) stent-graft 3.

As summarized in Figure 36, the largest FRZ is found in *stent-graft 2* (diverging diameter branch stent-grafts) (Figure 36.B). The smallest FRZ is observed in the model where the diameter of the branch stent-grafts matched the one of the vessels – *stent graft 1* (Figure 36.A).

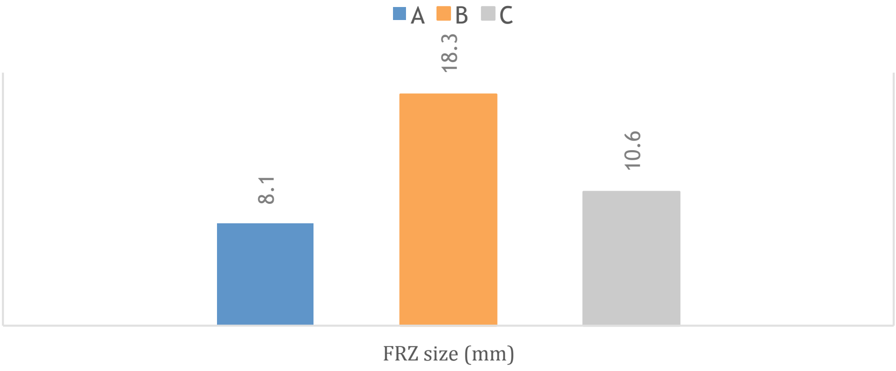

Figure 36 – Lengths of the flow recirculation zone, FRZ, found in the bypass of the LSCA through the LCCA in the geometries including a branched stent-graft: (A) stent-graft 1, (B) stent-graft 2, (C) stent-graft 3.

4.2 Discussion

The main objective of this work was to analyse the blood flow in an idealized prototype of a branched stent-graft for the endovascular repair of the aortic arch, using CFD methods. With this purpose, a new and easy methodology for a resistance type outflow boundary condition was implemented. The optimization of the stent-graft design for the best haemodynamic performance was also assessed.

Resistance type outflow boundary conditions were implemented in all four outlets of the models, using the methodology described in Chapter 3. Initial CFD simulations with an aortic arch model constructed with physiological dimensions, based on the aortic arch mapping reported by Finlay *et al.* [5], were performed and used as a *reference case*. Comparisons were performed with simulations in modified geometries of the aortic arch, including a branched stent-graft with a bypass of the LSCA through the LCCA, in order to access the haemodynamic performance of the device. Different branched stent-grafts, consisting of a main body with two branches for the IA an LCCA, were tested to study the impact of the diameter of the branches for the supra-aortic vessels on the flow characteristics.

4.2.1 Resistance type outflow boundary condition

Volumetric flow rate waveforms obtained at the outlet of the three supra-aortic vessels of the aortic arch model, in the simulations performed prescribing resistance type outflow boundary conditions, captured the main physiological flow features. They follow the same trend observed in the original flow waveforms corresponding to patient PC-MRI data, indicating the accuracy of this boundary condition. Results obtained for the blood inflow into the outlets of the models, as well as the mean values of the flow rates, were also significantly similar, when the resistance type outflow boundary condition was prescribed.

Comparing the physiological waveforms from patient-specific PC-MRI data with the ones obtained when performing simulations with the idealized geometry of the aortic arch, a decrease in the magnitude of the flow rate in the supra-aortic vessels was observed. Such result may arise from the simplification in the geometry that did not take into account the real curvature of the aortic arch. In fact, as has been reported by several authors [2, 19-21, 23, 36, 37], the curvature of the region promotes the blood inflow through the supra-aortic vessels, due to its skeweness, initially towards the inner wall and then to the outer wall of the aortic arch.

The similarity between the flow results obtained using the resistance type outflow boundary condition and the PC-MRI data from a patient was expected since the flow split into each vessel is dictated by the demands of the downstream arterial tree. Thus, prescribing the resistance imposed by the downstream vasculature at the outlets, a realistic description of blood flow is ensured. It is important to note that, in order to maintain the flow demand of the downstream vasculature, the pressure waveform has to change accordingly.

In fact, when resistance type outflow boundary conditions were prescribed, the physiological phase lag between the flow and the pressure waveforms was not observed. The shape of the pressure waveform is similar to that of the flow waveform, as prescribed by the relationship between flow and pressure, Equation 3.3. Thus, although using this methodology for resistance type outflow boundary conditions yields physiological flow results, those are obtained at the expense of the temporal dependence of the pressure waveform.

The specific resistance hold constant for all simulations (with and without stent-grafts), and periodicity was achieved in all within three cardiac cycles. Such results suggest that the methodology used in this work is, in fact, a fast and robust method of easily implementing a resistance type boundary condition.

4.2.2 Branched stent-grafts for the aortic arch

Branched stent-grafts consist of a main body stent-graft with fixed branches of specific dimensions that can be oriented into the vessels of the aortic arch, making them adaptable to a wide variety of anatomical geometries, while eliminating the need for customization. However, commercially available stent-grafts can only be manufactured in a small range of dimensions that may not fit perfectly the patient’s anatomy. The primarily aim of this work was precisely to use CFD simulations to evaluate the hemodynamic consequences of endovascular reparation of the aortic arch using branched stent-grafts and to study the impact of the diameter of the branches for the supra-aortic vessels on the flow characteristics.

The simulations results suggest that stent-grafts increase blood perfusion through the three supra-aortic vessels, and, by consequence, there is a slight decrease of the amount of blood flowing through the descending aorta. Such behaviour is mainly due to the presence of the branches of the stent-graft, which act as tunnels directing the blood flow through the vessels as a result of their protrusion into the main body of the stent-graft. This is a very interesting result since the major concern, when performing EVAR of the aortic arch, is the need to ensure blood perfusion to the upper parts of the body.

Results indicate that the presence of the stent-graft drastically increase the magnitude of the wall shear stress, since higher time-averaged values were found in the models including the branched stent-graft. For the post-operative geometries, the higher TAWSS values were observed at the walls of *stent-graft 2*, when the branch stent-grafts are diverging tunnels, while the lowest was found in *stent-graft 3*. High wall shear stresses are associated with higher displacement forces experienced by the stent-grafts [17]. Since large displacement forces are strongly related to future migration of the stent-grafts after surgery, the drastically increase of the TAWSS observed for the stent-grafted geometries should be carefully access, namely through the quantification of the displacement forces, to ensure that post-operative complications, such as migration of the device, do not arise.

Helical blood flow patterns were observed in all four models of the aortic arch (without and with branched stent-graft) during the mid-deceleration time-point of the cardiac cycle ($t = 0.21$ s). Such result is consistent with blood flow patterns in a healthy aorta reported by several authors: blood flow ranges from axial during the first part of the systole, to helical in its mid-to-late portion, with complex flow recirculation at the end of the systole and at diastole [8, 34].

Persistent FRZ were identified in the proximal wall of the bypass of the LSCA through the LCCA, with the largest ones being observed at the mid-deceleration time-point ($t = 0.21$ s). In FRZ, the flow is disturbed, causing regions of low WSS, parameter that has been reported to be associated with the formation of atherosclerotic plaques [2, 9, 17, 19]. Therefore, the presence of FRZ may be favourable to the development of thrombus, leading to partial, or even complete, occlusion of the bypass, preventing blood perfusion through the LSCA, which could result in ischemia of the left upper part of the patient’s body. This is the reason why FRZ should be avoided.

The FRZ was found to be significantly larger in the model where the branch stent-grafts consisted in diverging diameter tunnels for both the IA and LCCA, followed by the one where the branch stent-grafts consisted in a converging diameter tunnel for the IA and a diverging one for the LCCA. The smallest FRZ was found in the geometry where the diameter of the branch stent-graft was equal to the one of the vessels. As expected, such results suggest that the best haemodynamic performance would be achieved with customized branched stent-grafts whose branches dimensions matched the ones of the patient’s vessels. As an off-the-shelf device is intended, in order to minimize delays and cost, according to the results obtained, preference should be given to branches with slightly higher diameters than the ones of the vessels (converging diameter tunnels) as these yield smaller FRZ in the bypass.

In this work, a simplification of the geometry of the aortic arch was considered, neglecting the sites curvature and non-planarity. Since these two geometric parameters have been reported to be responsible for the helical and retrograde flow patterns observed in this anatomical region, further studies should be performed to include them and access their impact on the results. As the flow through the supra-aortic vessels in a healthy aortic arch is largely promoted by its curvature, a combination of this geometric parameter with the tunnels from the branched stent-graft is expected to favour the inflow split into the supra-aortic vessels. Nevertheless, this work provides a basic understanding of the flow characteristics, and its dependence on geometric parameters of the stent-graft as it was intended.

5 Conclusions

5.1 Main conclusions

In this work, the blood flow in simplified three-dimensional models of the aortic arch, with its three upper branches, before and after the introduction of an idealized branched stent-graft, was analysed, using numerical methods. Flow rate waveforms, flow split into the outlets and mean flow rates were extracted and compared. The presence of the stent-grafts increases blood perfusion through the three supra-aortic vessels, ensuring blood perfusion to the upper parts of the body.

The introduction of the stent-graft drastically increases the magnitude of the wall shear stress. Such observation should be carefully assessed, namely through the quantification of the displacement forces associated to higher wall shear stresses, in order to ensure that post-operative complications do not arise.

In the numerical analysis, a new and easy to implement methodology for a resistance type outflow boundary condition, consisting in the attachment of a constriction tube to the outlets of the models, imposing the resistance of the downstream vasculature, was also tested.

Volumetric flow rate waveforms obtained in the simulations, where resistance type outflow boundary conditions were prescribed, capture the main physiological flow features, and follow the trend observed in patient PC-MRI data. Nevertheless, a decrease in the flow rate magnitude is observed, possibly due to simplifications in the geometry, where the real curvature of the aortic arch was neglected.

The specific resistance held constant in all simulations (with and without stent-grafts), and periodicity was achieved in all within three cardiac cycles, suggesting that the methodology used is, in fact, a fast and robust method of easy implementation of a resistance type boundary condition.

Three branched stent-grafts were tested, in order to evaluate the impact of the diameter of the stent-graft’s branches in the hemodynamic performance of the device. No significant differences, in the flow rate waveforms, mean flow rate values and the flow split, were found between the three stent-graft geometries.

A persistent flow recirculation zone was identified in the proximal wall of the bypass of the LSCA through the LCCA, with the largest being observed in the model where the branch stent-grafts consists in diverging diameter tunnels for both the IA and LCCA. The smallest FRZ was found when the diameter of the branch stent-graft is equal to the one of the vessels. FRZ should be avoided, since they may be favourable to the development of thrombus, leading to partial or even complete occlusion of the bypass, which can result in ischemia of the left upper part of the body.

Although the best haemodynamic performance will be achieved with customized branched stent-grafts, in order to minimize delays and cost in their manufacturing, preference should be given to branches with slightly higher diameters than the ones of the vessels (converging diameter tunnels) as these yield smaller FRZ in the bypass.

5.2 Limitations and Future work

The main limitation in this work relates to the simplification in the geometry, where the curvature and non-planarity of the aortic arch was neglected. Since these two geometric parameters have been reported to be responsible for the helical and retrograde flow patterns observed in this anatomical region, further studies should be performed in order to access their impact on the results, *e.g.*, mean flow rates and blood inflow split for each outlet. Nevertheless, as the flow through the supra-aortic vessels, in a healthy aortic arch, is largely promoted by its curvature, a combination of this geometric parameter with the tunnels from the branched stent-graft presented in this work is expected to favour the inflow split into the three vessels.

In a future detailed study on the haemodynamic performance of the stent-graft, quantification of the displacement forces should be carried out. The study of this parameter will shed some light on the impact of the increase of the wall shear stresses observed for the stent-grafted geometries and its implications, usually related with post-operative complications, such as migration of the device.

5.3 Global statement

This work provides a basic understanding of the flow characteristics in an idealized branched stent-graft, and its dependence on geometric parameters of the device, as it was intended. A new, robust and easy to implement methodology for a resistance type outflow boundary condition was used, yielding physiological results.

References

1. World Health Organization. *Cardiovascular diseases (CVDs)*. Accessed in June 2015; Available from: http://www.who.int/mediacentre/factsheets/fs317/en/.
2. Ku, D.N., *Blood flow in arteries*. Annual Review of Fluid Mechanics, 1997. **29**: p. 399-434.
3. Shirakawa, Y., et al., *The efficacy and short-term results of hybrid thoracic endovascular repair into the ascending aorta for aortic arch pathologies*. Eur J Cardiothorac Surg, 2014. **45**(2): p. 298-304; discussion 304.
4. Moulakakis, K.G., et al., *The chimney-graft technique for preserving supra-aortic branches: a review*. Ann Cardiothorac Surg, 2013. **2**(3): p. 339-46.
5. Finlay, A., M. Johnson, and T.L. Forbes, *Surgically relevant aortic arch mapping using computed tomography*. Ann Vasc Surg, 2012. **26**(4): p. 483-90.
6. Gray, H., *Gray's Anatomy* 2005: Elsevier Limited.
7. Kousera, C.A., *A Numerical Study of Laminar-Turbulent Transition in Models of Canine and Human Aortas*, in *Department of Chemical Engineering and Chemical Technology*. 2010, Imperial College London.
8. Tan, F.P.P., et al., *Analysis of flow patterns in a patient-specific thoracic aortic aneurysm model*. Computers & Structures, 2009. **87**(11–12): p. 680-690.
9. Duraiswamy, N., et al., *Stented artery flow patterns and their effects on the artery wall*. Annual Review of Fluid Mechanics, 2007. **39**: p. 357-382.
10. Mancini, M.C. *Aortic Dissection*. December 5, 2014.
11. Cheng, Z., et al., *Predicting flow in aortic dissection: Comparison of computational model with PC-MRI velocity measurements*. Medical Engineering & Physics, 2014. **36**(9): p. 1176-1184.
12. The Hanckensack University Medical Center - Thoracic Aortic Aneurysm Program. *Type A Aortic Dissection*. Accessed in March 2015; Available from: http://www.aortarepair.com/type-a-aortic-dissection.html.
13. Ishimaru, S., *Endografting of the aortic arch*. J Endovasc Ther, 2004. **11 Suppl 2**: p. Ii62-71.
14. Kuratani, T., *Best surgical option for arch extension of type B dissection: the endovascular approach*. Ann Cardiothorac Surg, 2014. **3**(3): p. 292-9.
15. Inoue, K., et al., *Clinical application of transluminal endovascular graft placement for aortic aneurysms*. Ann Thorac Surg, 1997. **63**(2): p. 522-8.
16. Chuter, T.A., et al., *Modular branched stent graft for endovascular repair of aortic arch aneurysm and dissection*. J Vasc Surg, 2003. **38**(4): p. 859-63.
17. Kandail, H., M. Hamady, and X.Y. Xu, *Comparison of Blood Flow in Branched and Fenestrated Stent-Grafts for Endovascular Repair of Abdominal Aortic Aneurysms*. Journal of Endovascular Therapy, 2015.
18. Yokoi, Y., T. Azuma, and K. Yamazaki, *Advantage of a precurved fenestrated endograft for aortic arch disease: simplified arch aneurysm treatment in Japan 2010 and 2011*. J Thorac Cardiovasc Surg, 2013. **145**(3 Suppl): p. S103-9.
19. Caballero, A.D. and S. Laín, *A Review on Computational Fluid Dynamics Modelling in Human Thoracic Aorta*. Cardiovascular Engineering and Technology, 2013. **4**(2): p. 103-130.

20. Shahcheraghi, N., et al., *Unsteady and Three-Dimensional Simulation of Blood Flow in the Human Aortic Arch*. Journal of Biomechanical Engineering, 2002. **124**(4): p. 378-387.

21. Taewon, S., et al. *The blood flow simulations of human aortic arch model with major branches*. in *Biomedical Engineering and Informatics (BMEI), 2011 4th International Conference on*. 2011.

22. Vasava, P., et al., *Finite Element Modelling of Pulsatile Blood Flow in Idealized Model of Human Aortic Arch: Study of Hypotension and Hypertension*. Computational and Mathematical Methods in Medicine, 2012. **2012**: p. 861837.

23. Rui-Hung, K., et al. *Numerical simulation of blood flow crossing the aortic arch*. in *Orange Technologies (ICOT), 2013 International Conference on*. 2013.

24. Fung, G.S., et al., *On stent-graft models in thoracic aortic endovascular repair: a computational investigation of the hemodynamic factors*. Comput Biol Med, 2008. **38**(4): p. 484-9.

25. Vignon-Clementel, I.E., et al., *Outflow boundary conditions for three-dimensional finite element modeling of blood flow and pressure in arteries*. Computer Methods in Applied Mechanics and Engineering, 2006. **195**(29–32): p. 3776-3796.

26. Krsmanovic, D., et al., *Computer modelling of maximal displacement forces in endoluminal thoracic aortic stent graft*. Comput Methods Biomech Biomed Engin, 2014. **17**(9): p. 1012-20.

27. Pasta, S., et al., *Computer modeling for the prediction of thoracic aortic stent graft collapse*. J Vasc Surg, 2013. **57**(5): p. 1353-61.

28. van Prehn, J., et al., *Toward endografting of the ascending aorta: insight into dynamics using dynamic cine-CTA*. J Endovasc Ther, 2007. **14**(4): p. 551-60.

29. Benim, A.C., et al., *Simulation of blood flow in human aorta with emphasis on outlet boundary conditions*. Applied Mathematical Modelling, 2011. **35**(7): p. 3175-3188.

30. Lam, S.K., et al., *A computational investigation on the effect of biomechanical factors related to stent-graft models in the thoracic aorta*. Conf Proc IEEE Eng Med Biol Soc, 2007. **2007**: p. 943-6.

31. Stein, P., Sabbah, H., *Turbulent blood-flow in ascending aorta of humans with normal and diseased aortic valves*. Circulation Research, 1976. **39**(1): p. 58.

32. Kilner, P., Henein, M., Gibson, D., *Our tortuous heart in dynamic mode - an echocardiographic study of mitral flow and movement in exercising subjects*. Heart and Vessels, 1997. **12**(3): p. 103.

33. Campos, J.B.L.M.d., *Notas para o Estudo da Mecânica dos Fluidos*. 2013.

34. Kousera, C.A., et al., *A Numerical Study of Aortic Flow Stability and Comparison With In Vivo Flow Measurements*. Journal of Biomechanical Engineering, 2012. **135**(1): p. 011003-011003.

35. Womersley, J.R., *XXIV. Oscillatory motion of a viscous liquid in a thin-walled elastic tube—I: The linear approximation for long waves*. The London, Edinburgh, and Dublin Philosophical Magazine and Journal of Science, 1955. **46**(373): p. 199-221.

36. Seed, W., Wood, N., *Velocity patterns in aorta*. Cardiovascular Research, 1971. **5**(3): p. 319.

37. Nerem, R., Wood, N., Seed, W., *Experimental study of the velocity distribution and transition to turbulence in aorta*. Journal of Fluid Mechanics 1972. **52**(MAR14): p. 137.

38. Pedley, T.J., *The Fluid Mechanics of Large Blood Vessels*. 1980: Cambridge University Press.

39. Xiao, N., *Simulation of 3-D Blood Flow in the Full Systemic Arterial Tree and Computational Framework for Efficient Parameter Estimation*, in *Department od Bioengineering* 2014, Stanford University.

40. Pahlevan, N., et al., *A Physiologically Relevant, Simple Outflow Boundary Model for Truncated Vasculature*. Annals of Biomedical Engineering, 2011. **39**(5): p. 1470-1481.

41. Olufsen, M., et al., *Numerical Simulation and Experimental Validation of Blood Flow in Arteries with Structured-Tree Outflow Conditions*. Annals of Biomedical Engineering, 2000. **28**(11): p. 1281-1299.

Appendix

I. Tables

Table A. 1 - Dimension of the geometric parameters used to describe the fluid domain. Models of the aortic arch including stent-graft: (A) stent-graft 1, (B) stent-graft 2, (C) stent-graft 3.

Parameter (mm)	**Model of the aortic arch**		
Inlet diameter	32		
Outlet diameter	28		
Total length	150		
Length of the constant diameter section	100		
Length of the tapered section	50		
IA diameter	15		
LCCA diameter	9.5		
LSCA diameter	13		
IA, LCCA and LSCA length	20		
Distance between IA and LCCA	5.5		
Distance between LCCA and LSCA	8		
Distance between inlet and IA	15		
Distance of LCCA anterior to IA and LSCA	4		
Modified geometries including the branched stent-graft			
Parameter (mm)	**(A)**	**(B)**	**(C)**
IA branch stent-graft diameter	15	8	10
LCCA branch stent-graft diameter	9.5	8	10
Height of the LSCA bypass on the LCCA	20		

Table A. 2 - Mesh statistics for all geometries: (A) the aortic arch model without stent-graft, and the models including the branched stent-graft: (B) stent-graft 1, (C) stent-graft 2, (D) stent-graft 3.

Geometry	**Aortic arch model (A)**	**Modified geometries including the branched stent-graft**		
		(B)	**(C)**	**(D)**
Number of nodes	293 824	978 514	959 829	973 331
Number of elements	851 224	3 636 988	3 575 606	3 623 894

II. Calculations

Determination of the peak systole Reynolds number and Womersley parameter:

For a vessel with an inlet diameter of $d_{inlet} = 32\ \mathrm{mm}$, the cross-sectional area of the inlet is given by:

$$S = \Pi\left(\frac{d_{inlet}}{2}\right)^2 = \Pi\left(\frac{0.032\ \mathrm{m}}{2}\right)^2 = 8{,}0 \times 10^{-4}\ \mathrm{m}^2\ ,$$

and the mean velocity at the inlet can be determined as follows:

$$\bar{u} = \frac{\hat{Q}}{S}\,,$$

where $\hat{Q}$ is the peak systole volumetric flow rate. The value of $\hat{Q}$ can be extracted from the volumetric flow rate waveform at the ascending thoracic aorta (Figure 10, in Chapter 3):

$$\hat{Q} = 500\ \frac{\mathrm{cm}^3}{\mathrm{s}} = 5{,}00 \times 10^{-4}\,\frac{\mathrm{m}^3}{\mathrm{s}}\,.$$

Assuming blood to be a Newtonian fluid, with a density, ρ, of 1 060 kg/m^3 and a constant dynamic viscosity, μ, of 0.004 Pa.s, the peak Reynolds number, $\widehat{\mathrm{Re}}$, can be determined as follows:

$$\widehat{\mathrm{Re}} = \frac{\rho.\bar{u}.d_{inlet}}{\mu} = \frac{\rho.\left(\hat{Q}/S\right).d_{inlet}}{\mu} = 52\,727\ .$$

On its turn, the Womersley parameter, α, is given by:

$$\alpha = \frac{d_{inlet}}{2}\sqrt{\frac{\omega}{\upsilon}} = \frac{d_{inlet}}{2}\sqrt{\frac{2\Pi/\mathrm{T}}{\rho/\mu}} = 23.7\,,$$

where ω is the cardiac frequency, υ is the kinematic viscosity and T the period of the volumetric flow waveform, *i.e.*, the duration of one cardiac cycle, 0.76 s.